THE USE OF COPPER PHYLLOSILICATE AS A SUPPORTED TEMPLATE TO PREPARE WO_3/SIO_2 CATALYST FOR CROSS-METATHESIS OF ACETYLENE AND ETHYLENE

KANOKWAN WENGWIRAT

A THESIS SUBMITTED IN PARTIAL FULFILLMENT OF THE REQUIREMENT FOR THE DEGREE OF MASTER OF SCIENCE IN APPLIED CHEMISTRY

DEPARTMENT OF CHEMISTRY SCHOOL OF SCIENCE
KING MONGKUT'S INSTITUTE OF TECHNOLOGY LADKRABANG

2025
KMITL-2025-SC-M-012-018

Thesis Title	The use of copper phyllosilicate as a supported template to prepare WO_3/SiO_2 catalyst for cross-metathesis of acetylene and ethylene
Student Name	Kanokwan Wengwirat
Student ID	64605004
Degree Department	Master of Science (Applied Chemistry)
Year	2025
Thesis Advisor	Assoc. Prof. Dr. Kittisak Choojun
Thesis Co-advisor	Prof. Dr. Tawan Sooknoi

Abstract

Bio-butadiene can be produced from cross-metathesis of bioethanol-derived acetylene/ethylene over supported WO_3 on silanol-rich silica prepared with Cu-leached copper phyllosilicates (CuPS). 20CuPS and 30CuPS were preliminarily reduced before Cu-leaching under an acidic solution (1 M HCl). Compared with fumed SiO_2, ^{29}Si CPMAS NMR spectroscopy showed an increase in surface silanols, particularly the isolated silanols (Q_3), from removing Cu^{2+} octahedral sites ($Cu^{2+}(OSi)_6$) encapsulated within tetrahedral silica layers of CuPS. The surface silanols in fumed SiO_2, 20CuPS-Le, and 30CuPS-Le adequately accommodate single-site and polymeric WO_3 species, leading to a similar 1,3-butadiene production rate (~4.7 mmol/h·g_{cat}) at 5wt.% loading. Only 30CuPS-Le sufficiently provides the exposed silanols to disperse 8wt.% WO_3 loading without bulk WO_3 formation. The cross-metathesis activity depends on the relative amounts of exposed silanols. Accordingly, the steady 1,3-butadiene production was obtained in the order of $8WO_3$/30CuPS-Le (6.3 mmol/h·g_{cat}) > $8WO_3$/20CuPS-Le (5.1 mmol/h·g_{cat}) > $8WO_3/SiO_2$ (2.5 mmol/h·g_{cat}).

Keyword: Cross-metathesis; Copper phyllosilicate; Acetylene; Bio-butadiene; Tungsten oxide catalyst

Acknowledgement

I would like to express my sincere appreciation to my advisors, Assoc. Prof. Dr. Kittisak Choojun and co-advisor Prof. Dr. Tawan Sooknoi, for their guidance, encouragement, and valuable advice throughout my research. Without their support and constructive feedback, this thesis would not have been complete. I would also like to extend my heartful gratitude to the chairperson, Assoc. Prof. Dr. Chularat Wattanakit, as well as the committee member, Assoc. Prof. Dr. Karoon Sadorn, for their valuable feedback and helpful suggestions that have significantly improved this work.

This research was generously supported by of King Mongkut's Institute of Technology Ladkrabang (KMITL) and funding provided by the National Research Council of Thailand (NRCT) and King Mongkut's Institute of Technology Ladkrabang, Thailand:(N42A660796), School of Science, King Mongkut's Institute of Technology Ladkrabang, Thailand (Grant Nos. RA/TA-2564-M-004), and National Research Council of Thailand (NRCT). I am deeply grateful to Synchrotron Light Research Institute (Public Organization), Thailand, for the EXAFS experiments at beamlines 5.2 and 8 and the Scientific Instruments Center, School of Science, KMITL for their kind assistance and provision of access to advanced analytical instruments essential for the characterization processes. I would like to extend my thanks to the members of the Catalysis Research Unit for their continuous support, insightful discussions, and kind encouragement throughout this journey.

Furthermore, I am deeply grateful to the Department of Chemistry, School of Science, King Mongkut's Institute of Technology Ladkrabang, for providing access to laboratory instruments, equipment, chemicals, and research facilities

Finally, I would like to express my heartfelt thanks to my family for their love, support, and understanding. Their belief in me has been my greatest motivation.

Miss Kanokwan Wengwirat

Table of contents

Table of contents (continued)

List of tables

List of figures

List of figures (continued)

List of schemes

Abbreviations/Symbols

°C	Degree Celsius
CuPS	Copper phyllosilicate
CuPS-Le	Cu-leached Copper phyllosilicate
BET	Brunauer-Emmett-Teller method
CPMAS NMR	Cross-Polarization Magic Angle Spinning Nuclear Magnetic Resonance
DR-UV	Diffuse reflectance UV-VIS spectrophotometer
EXAFS	Extended X-ray Absorption Fine Structure
FID	Flame Ionization Detection
ICP-OES	Inductively Coupled Plasma Optical Emission spectroscopy
SEM	Scanning Electron Microscope
XANES	X-ray Absorption Near Edge Structure
XRD	X-Ray Diffraction
WD-XRF	Wavelength Dispersive X-ray fluorescence spectrophotometer

CHAPTER 1
Introduction

1.1 Research motivation

Butadiene serves as a key feedstock for the production of butadiene rubber (BR) and styrene-butadiene rubber (SBR), which are widely utilized in the manufacturing of tires, automotive components, adhesives, coatings, and consumer goods [1–6]. The global demand for butadiene reached approximately 12 million tonnes in 2022 [7]. Generally, butadiene is produced via petrochemical processes such as butene dehydrogenation [8,9], naphtha steam cracking [10–12], and ethylene conversion [13–15], all of which raise concerns regarding carbon neutrality. An alternative approach involves producing butadiene via the dehydration of butanol, which is derived from the Güerbet reaction of bioethanol. This method enhanced carbon efficiency and sustainability. However, this method suffers from low selectivity and catalyst deactivation [16,17].

An alternative sustainable method for butadiene production involves the cross-metathesis between bio-ethylene and bio-acetylene, which can be derived from bioethanol dehydration/dehydrogenation and carbon-to-acetylene coupling with CO_2 capture [18–23]. Trotus *et al.* demonstrated that the ruthenium carbene complex (HG2) achieved a high selectivity of up to ~70% for 1,3-butadiene via acetylene/ethylene cross-metathesis [24]. However, this reaction requires high pressure (11–14 bar), and the catalyst undergoes deactivation due to acetylene polymerization. Recently, Promchana *et al.* reported that silica-supported WO_3 exhibited high butadiene selectivity (>80%) and stability in acetylene/ethylene cross-metathesis [25]. The formation of active single-site WO_3 species on silica supports, such as mono-oxo ($(O=)W(O\text{-}Si)_4$) and di-oxo ($(O=)_2W(O\text{-}Si)_2$), is influenced by the quantity and type of silanols, particularly isolated and geminal silanols [26,27]. Although confined SiO_2 supports such as MCM-41, SBA-15, and silicalite-1 provide highly isolated silanols, their synthesis is quite expensive, primarily due to the requirement of organic templates.

Alternatively, phyllosilicate (PS), a silica-based layered material incorporating metal ions (M^{n+} = Cu^{2+}, Ni^{2+}, Co^{2+}) within its octahedral structure, can serve as a silanol-rich support and can be synthesized without the need for organic templates.

It is anticipated that a high concentration of isolated and geminal silanols can be exposed upon the removal of metal ions from the octahedral sites ($M^{n+}(Osi)_6$), which are embedded within tetrahedral silica layers (chrysocolla structure, shown in **Scheme 1.1**). Consequently, the metal-leached phyllosilicate, characterized by a high silanol density, could accommodate a greater dispersion of single-site WO_3 species. The initial copper loading likely influences the surface area and the concentration of exposed silanols [28–31].

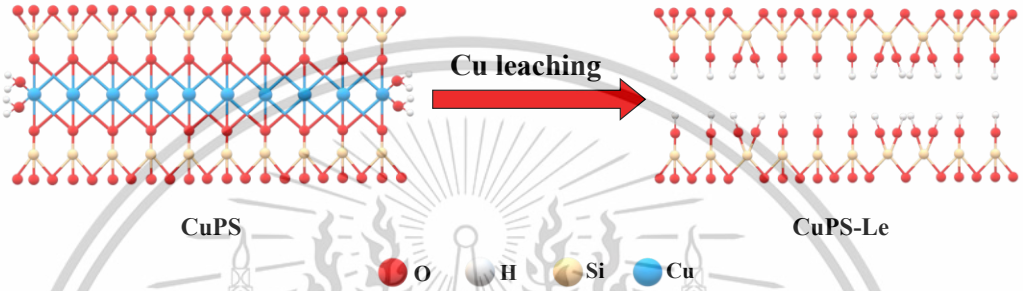

Scheme 1.1. Illustration of additional exposure of isolated and geminal silanol groups following the leaching of metal ions from phyllosilicates (PS).

Thus, this project aims to investigate the use of copper phyllosilicate (CuPS) as a silica template for supported WO_3 catalysts for cross-metathesis of acetylene and ethylene compared with fumed SiO_2. The reaction will be performed in a continuous fixed-bed reactor under atmospheric pressure. As reported in the literature, the CuPS with 20 and 30 wt.% Cu loading will be synthesized via the ammonia-evaporation hydrothermal method [29]. The effect of CuPS reduction temperature at 250 °C will be investigated. All reduced CuPS samples will be treated with 1.0 M HCl at 60 °C for 1 h in order to leach the Cu. The 5 and 8 wt.% of WO_3 loadings will be impregnated over the leached CuPS and fumed SiO_2 using ammonium metatungstate tetrahydrate as a precursor. The sample will be characterized by XRD, XRF, ICP-OES, BET, SEM, EXAFS, and solid-state ^{29}Si CPMAS NMR. The formation of WO_3 species will be examined by Raman spectroscopy and DR-UV adsorption. The acetylene/ethylene cross-metathesis will perform a reaction at 450 °C and pathway will be studied.

1.2 Objectives of the study

1.2.1 To obtain 1,3-butadiene from the metathesis of acetylene and ethylene over supported tungsten oxide on siliceous catalysts.

1.2.2 To compare the activity of supported WO_3/SiO_2 catalysts prepared by SiO_2 from CuPS template compared with fumed SiO_2.

1.2.3 To understand the effect of surface silanols (Si-OH) generated from the CuPS template on the formation of WO_3 species.

1.3 Scopes of study

1.3.1 The CuPS with 20 and 30wt.% Cu loading will be synthesized via the ammonia-evaporation hydrothermal method.

1.3.2 The CuPS will be reduced at 250°C under H_2 with a heating rate of 10 °C/min for 2 h and will be treated with 1 M HCl, yielding the SiO_2 from the CuPS template.

1.3.3 Synthesis of supported tungsten oxide on SiO_2 from CuPS template and fumed SiO_2 by incipient wetness impregnation method with the WO_3 loadings of 5, 8 wt.%.

1.3.4 Characterization of catalysts by X-ray diffraction (XRD), X-ray fluorescence (XRF), Inductively Coupled Plasma Optical Emission spectroscopy (ICP-OES), N_2 adsorption-desorption (BET), Scanning Electron Microscope (SEM), Diffuse reflectance ultraviolet-visible spectroscopy (DR-UV), Solid-state silicon Magic Angle Spinning Nuclear Magnetic Resonance Spectroscopy (solid-state ^{29}Si CPMAS NMR), Extended X-ray Absorption Fine Structure (EXAFS) and Raman spectroscopy.

1.3.5 The gas products from the reactions will be qualitatively and quantitatively analyzed by using a gas chromatograph (GC-FID).

1.4 Benefits of study

This study could provide new supported tungsten oxide catalysts for metathesis reactions. Furthermore, this study could support the industrial platform for butadiene production.

CHAPTER 2

Theory and Literature reviews

2.1 Olefin metathesis

Olefin metathesis is an organic reaction that entails the rearrangement of fragments of alkenes (olefins) by the scission and regeneration of carbon-carbon double bonds [32]. Olefin metathesis can be categorized as cross-metathesis (CM), ring-opening metathesis (ROM), ring-closing metathesis (RCM), ring-opening metathesis polymerization (ROMP), acyclic diene metathesis (ADMET) [33]. The metathesis reaction requires a transition metal carbene as the active species with a vacant coordination site at the transition metal center. The initial metal carbene can be formed by a reaction between the catalyst and the co-catalyst, if present, or by the substrate olefins interaction with the transition metal center. The olefins will coordinate at this vacant site and subsequently form a metallacyclobutane intermediate. This metalacyclic obtains the new olefin, which contains an alkylidene fragment from the catalyst and the other one from the starting olefin. The new metal-alkylidene complex can re-enter into a catalytic cycle, as shown in **Figure 2.1**.

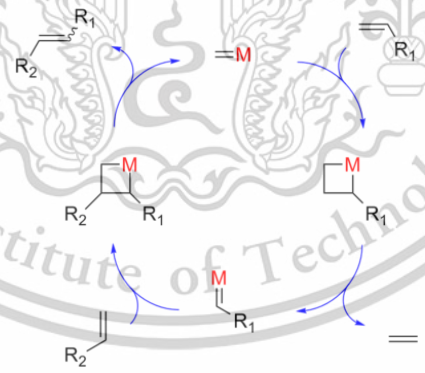

Figure 2.1 Catalytic cycle of metathesis reaction

2.1.1 Cross-Metathesis

Cross-metathesis involves the intermolecular reaction of two alkene units [58]. For instance, the cross-metathesis of alkyne with olefins provides a route to produce higher olefins with two double bonds in molecules. Meanwhile, the reaction with

ethylene, often referred to as enyne metathesis as shown in **Figure 2.2**, has become an essential method for the synthesis of intermediates for chemical productions [34].

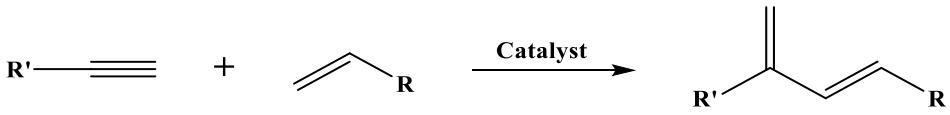

Figure 2.2 Enyne metathesis of alkyne and ethylene.

2.2 Acetylene

Acetylene (C_2H_2), the simplest alkyne, is a linear molecule consisting of two carbon atoms connected by a triple bond, resulting in a bond angle of 180°. This structure imparts high unsaturation and reactivity, making acetylene a valuable building block in both combustion and synthetic organic chemistry. It is a colorless, flammable gas thermodynamically unstable in its pure form, sensitive to exothermic decomposition above 1 bar when subjected to mechanical shock or elevated temperatures. Due to this instability, acetylene is commonly stored in solution, most notably in acetone or dimethylformamide (DMF) [35].

Acetylene is utilized across various industries, particularly in metalworking, where it enables high-temperature oxyacetylene welding and cutting, reaching over 3300 °C. Although partially replaced by arc-based techniques, it remains valuable in brazing, annealing, and remote field repairs. In chemical synthesis, acetylene is a key feedstock that produces precursors for rubber, vinyl fabric, and paints [36].

2.3 Ethylene

Ethylene (C_2H_4) is the simplest member of the alkene family, characterized by a carbon-carbon double bond. It is a colorless, flammable gas with a mildly sweet odor with a melting point of −170 °C and a boiling point of −100 °C. Naturally occurring in both petroleum and natural gas, ethylene is a plant hormone that regulates growth, induces leaf abscission, and promotes fruit ripening. Industrially, ethylene was produced through the thermal cracking of hydrocarbons such as ethane and propane at temperatures between 800–900 °C, followed by separation from the resulting gas mixture [37].

Ethylene plays a vital role in the chemical industry, primarily as a monomer and feedstock for other two-carbon compounds. Its most significant application is in the production of polyethylene through polymerization processes, which yield various types, including low-density polyethylene (LDPE) and high-density polyethylene (HDPE), depending on the conditions and catalysts used. Additionally, ethylene was employed in producing linear **α**-olefins via oligomerization, which serves as precursors for linear low-density polyethylene (LLDPE) and other valuable chemical products [38].

2.4 1,3-butadiene

1,3-Butadiene (C_4H_6) is a linear, unsaturated hydrocarbon belonging to the conjugated diene, featuring two alternating double bonds (C=C–C=C) within a four-carbon chain. This conjugated structure enhances its chemical reactivity, making it a vital raw material in synthetic rubber production, particularly in fabricating automotive tires. Traditionally, 1,3-butadiene was predominantly obtained through processes such as the dehydrogenation of butane or butenes [8,9] and the thermal cracking of petroleum-derived hydrocarbons [10–12].

At ambient conditions, 1,3-butadiene is a colorless gas that can be transformed into its liquid phase by cooling to –4.4 °C or compressing to approximately 2.8 bar at 25 °C. Its high reactivity allows it to undergo polymerization reactions, especially in the presence of catalysts, where it forms copolymers with monomers like styrene or acrylonitrile—key components in elastic, rubber-like materials. Furthermore, 1,3-butadiene engages in cycloaddition reactions, such as the Diels–Alder reaction with compounds like maleic anhydride, leading to the synthesis of six-membered ring products useful in advanced chemical manufacturing [39].

2.5 Diels-alder reaction

The Diels–Alder reaction is a [4+2] cycloaddition process that involves the interaction of a conjugated diene (providing four π-electrons) with a dienophile—typically an alkene or alkyne (contributing two π-electrons). The reaction is thermodynamically driven by the formation of two new σ-bonds, which are more stable than the π-bonds they replace. In cases involving alkynyl dienophiles, the resulting adduct can further participate as a dienophile, provided steric hindrance is

minimal [39]. The diene–dienophile interaction may also yield a substituted allene under certain conditions, although this product lacks a conjugated system. Renowned for its operational simplicity and efficiency, the Diels–Alder reaction is among the most widely employed methods for constructing six-membered unsaturated rings such as cyclohexene. Furthermore, it is adaptable to heteroatom-containing substrates, enabling the synthesis of six-membered heterocycles when either the diene or dienophile incorporates atoms such as nitrogen or oxygen [40].

2.6 Literature reviews

1,3-butadiene can be produced via several petrochemical processes such as butene dehydrogenation, naphtha steam cracking, ethylene conversion, and butanol dehydration.

Ishizaki *et al.* (2024) studied the performance of $Pt/SnO_2–Al_2O_3$ catalyst in the dehydrogenation of 1-butene in a fixed-bed reactor at 550 °C under atmospheric pressure [8]. The $7\%Sn_2$-Al_2O_3 support materials were prepared by impregnation using Al_2O_3 and $SnCl_2 \cdot H_2O$ as a precursor in ethanol solution. After calcined at 550 °C under air (100mL/min) for 3h and 800 °C for 3h in air flow, The calcined $SnO_2–Al_2O_3$ was impregnated with aqueous solution of 1 wt.% of H_2PtCl_4 then calcined at 550 °C under air and reduced at 550 °C under H_2 flow. The $1\%Pt/7\%$ Sn_2-Al_2O_3 catalyst showed 1-butene conversion of approximately 25% (at 20min) with selectivity to 1,3-butadiene around 90% after 2h on stream.

Yoshimura *et al.* (2001) reported that in a naphtha steam cracking process without a catalyst, operated in a fixed-bed reactor at 780–870 °C, 1,3-butadiene was obtained as a by-product with a yield of 4.6% [41]. Li *et al*. (2018) demonstrated using Mg_6MnO_8 doping with Praseodymium (Pr) for oxy-cracking of *n*-hexane in a continuous flow reactor. The catalyst was prepared by impregnating magnesium powder with a $Mn(NO_3)_2$ solution and calcined at 950 °C. Then, the prepared catalyst was doping with 5 wt.% loading Pr. At 775 °C with 150mL/min of 10% *n*-hexane/Argon, it resulted in a 1,3-butadiene yield of 4.2%, corresponding to a 72% conversion of *n*-hexane [42].

Il'chenko *et al*. (1994) studied the performance of an aluminosilicate catalyst for ethylene conversion in a flow reactor at 600-700 °C (total feed rate 50 ml/min of

3% ethylene/He) [14]. At 700 °C and 1 bar, the catalyst achieved 5.4% ethylene conversion with 43.2% selectivity of 1,3-butadiene. Dolgikh *et al*. (1995) report that 1,3-butadiene could be observed from ethylene conversion, even without a catalyst, in the flow reactor at 700-750 °C [15]. At 700 °C and 1 bar, a 5% ethylene conversion was observed with 50% selectivity of 1,3-butadiene.

Kruger *et al.* (2018) investigated the production of 1,3-butadiene through the integrated dehydration and dehydrogenation of 1-butanol in a fixed-bed reactor [43]. They achieved a yield of 15% for 1,3-butadiene from the butene dehydrogenation step by using a 1 wt% K-doped Cr_2O_3/Al_2O_3 catalyst positioned at the center of the reactor tube (at 450 °C). This dehydrogenation step followed the dehydration of 1-butanol, which was performed at 360 °C using an Al_2O_3 catalyst placed 5 inches above the center of the same reactor tube with a butanol flow rate of 0.02 mL/min and 177 mL/min of N_2. However, these methods suffer from low selectivity and raise concerns regarding carbon neutrality.

A sustainable alternative for butadiene production involves the cross-metathesis of ethylene with acetylene. Trotuş *et al.* (2015) reported that the use of homogenous catalysts, which is Hoveyda–Grubb's second-generation catalyst (HG2, **Figure 2.3**) for acetylene/ethylene cross-metathesis in the batch reactor at 40-80 °C (total pressure 11-14 bar, ethylene/acetylene = 32.5) [24]. At 60 °C, the HG2 showed a conversion of 80% with 70% cross-metathesis selectivity. However, the separation of products and recycling of homogenous catalysts limits their use in industries, particularly due to the relatively high cost of complex synthesis [44].

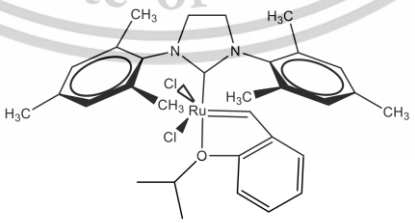

Figure 2.3 The 2nd generation Hoveyda-Grubb's complex [45].

Supported metal oxide catalysts, including Re, Mo, and W oxides, offer an easier and lower cost of synthesis [33]. Morrison *et al.* (2014) reported the use of

9%Re_2O_7/Al_2O_3 for the metathesis of 1-hexene to 5-decene. They performed the reaction in a fixed-bed reactor at 70 ℃, WHSV = 0.2 h^{-1} [46]. Even though the catalyst showed a high conversion at 87%, only 42.9% of 5-decene was obtained. In addition, C5-C9 products from the isomerization of 1-hexene were observed in 39% selectivity. Even though supported Re_2O_7 over Al_2O_3 and SiO_2-Al_2O_3 can perform cross-metathesis of 2-pentene and ethylene at 35-60 ˚C under 1 bar of ethylene [47], the sublimation of Re was observed during the calcination at 550℃ in air. In a similar manner, Bouchmella *et al*. (2015) mentioned that the Re sublimation was detected in Re-Si-Al catalysts upon calcination at 500 ˚C [48].

Supported Mo catalysts offer higher stability than Re-based catalysts. Zhang *et al.* (2012) reported catalytic performances of Mo/HβAl_2O_3, Mo/HMOR-Al_2O_3, and Mo/Al_2O_3 for metathesis of 1-butene and *iso*-butene in a continuous fixed-bed reactor under atmospheric pressure at 150 ˚C [49]. Catalysts with 6wt.%MoO_3 loading were prepared by impregnation using $(NH_4)_6Mo_7O_{24}{\cdot}4H_2O$ as a precursor. The impregnated samples were calcined at 600 ℃ for 2h. 6%Mo/Al_2O_3 offered high 1-butene and *iso*-butene conversions (45.3% and 30.7%). Rodríguez-Ramos *et al*. (1995) studied the metathesis of propylene to ethylene and butene using MoO_3/Al_2O_3 in a fixed-bed reactor at 300 ˚C under atmospheric pressure [50]. The catalysts were prepared by incipient wetness impregnation using $(NH_4)_6Mo_7O_{24}{\cdot}4H_2O$ solution, then calcined at 600 ℃ for 3h. Prior to use, the MoO_3/Al_2O_3 catalysts were pretreated in helium at 600 ℃ for 1h. The catalysts showed selectivity of ethylene and butene at 40 and 50%, respectively. They also reported that the catalytic activity increases with metal loading. However, at high loading (>10wt.%), the side reactions, including polymerization, isomerization and cracking were observed due to the acid sites from molybdenum catalysts. Even though MoO_3-based catalysts show a good metathesis performance, they are sensitive to oxygenates and moistures, leading to fast deactivation. In a similar manner, Rybak *et al*. (2008) mentioned that MoO_3 catalysts needed to be kept in an inert atmosphere [51].

Supported Tungsten oxide is resistant to poisoning by oxygenated impurities [52]. Debecker *et al.* (2014) reported that WO_3/Al_2O_3 can perform cross-metathesis of ethylene and 2-butene to propene in a continuous fixed-bed reactor at 250 ℃ under atmospheric pressure. The catalysts were prepared by the impregnation method using $H_3PW_{12}O_{40}$ as a precursor. At the equal molar ratio of ethylene: 2-butene, the catalyst

provided a 54% propene yield. However, side reactions, especially the isomerization were observed due to the acidity of the catalysts [53].

The use of the Hierarchical HY prepared by the dealuminated HY zeolite can improve the WO_3 dispersion with a lower acidity as compared to WO_3/Al_2O_3. Watmanee *et al.* (2019) investigated the formation of terminal tungsten sites over HY zeolite on propene metathesis [26]. The catalyst was pre-treatment under N_2 at 500˚C for 1h, and performed the reaction at 550˚C under 20% propene/N_2. They found that the synthesis of Hierarchical HY by dealuminated HY zeolite increases the terminal silanol group density, leading to high tungsten dispersion in the form of terminal tungsten (mono- and di-oxo tungsten). As a result, high metathesis products (60%) and decreased side reactions like isomerization and oligomerization. However, the remaining acidity in this catalyst still causes deactivation due to coke formation [54].

Alternatively, the use of confined SiO_2, including MCM-41 and SBA-15 as supports for WO_3 can decrease the acidity with high WO_3 dispersion and surface area. Bhuiyan *et al.* (2013) studied the metathesis of 2-butene using WO_3/SBA-15 and WO_3/MCM-41 [55]. The catalysts were prepared wet impregnation with an aqueous solution of ammonium metatungstete hydrate and calcined in air at 550 ℃ for 5h. The catalysts were treated in N_2 at 550˚C for 1h prior to use. The reaction was investigated at 200-500 ˚C for 5-12 h of time on stream (TOS). They found that WO_3/MCM-41 exhibited higher activity (2-butene conversion 87%) compared to WO_3/SBA-15 (2-butene conversion 80%) since better WO_3 dispersion was observed in MCM-41. Though, their synthesis is quite expensive, primarily due to the requirement of organic templates.

Amorphous silica (SiO2) has been proposed as a low-cost support material for tungsten oxide catalysts to address the high synthesis cost associated with the use of organic templates. In fact, SiO_2 lacks acidity. Accordingly, WO_3/SiO_2 was applied to the metathesis reaction. Lwin *et al.* (2016) studied propene metathesis over WO_3/SiO_2 (2, 4, 6, 8, and 20wt.%). The catalysts were prepared by the impregnation using ammonium metatungstate hydrate as a precursor. The samples were calcined under air-zero at 500 ℃ for 3h. They found that mono- and dioxo-WO_3 species ($(O=)W(O\text{-}Si)_4$, $(O=)_2W(O\text{-}Si)_2$) were mainly observed in WO_3/SiO_2 with 4 and 6wt.% WO_3 loadings, while crystalline WO_3 (bulk WO_3) were observed over the catalysts with ≥8wt.% WO_3 loading [54]. In line with this view, Lee and Wachs *et al.* (2007) examined the formation of

WO_3 species using the spectroscopy method. They discovered that the mono-oxo and di-oxo WO_3 were observed at lower 8wt.% WO_3 loading [56].

Promchana *et al.* (2023) studied WO_3 over SiO_2 at 2, 3, 5 and 7wt.% WO_3 loadings for acetylene/ethylene cross-metathesis [25]. They reported that 2%WO_3/SiO_2 composed of 4-coordinated, 5-coordinated mono-oxo ((O=) $W(O\text{-}Si)_3$, (O=) $W(O\text{-}Si)_4$) and di-oxo WO_3 species ($(O=)_2W(O\text{-}Si)_2$), while WO_3 cluster species were observed at 3-5%WO_3/SiO_2 and bulk WO_3 species were obtained in 7%WO_3/SiO_2 (**Figure 2.4**). They mentioned that WO_3 formation depended on the available silanols on the surface of supports. At a low WO_3 loading (2%WO_3/SiO_2), the silanol is sufficient to accommodate the incorporated WO_3 forming single-site WO_3 species, including mono-oxo and di-oxo WO_3 species. These species (2%WO_3/SiO_2, 53 h^{-1}) showed the highest activity for acetylene/ethylene cross-metathesis. Though, the catalysts with cluster and bulk species (3-7%WO_3/SiO_2) showed lower TOF. Thus, silanols play a crucial role to generate active WO_3 species.

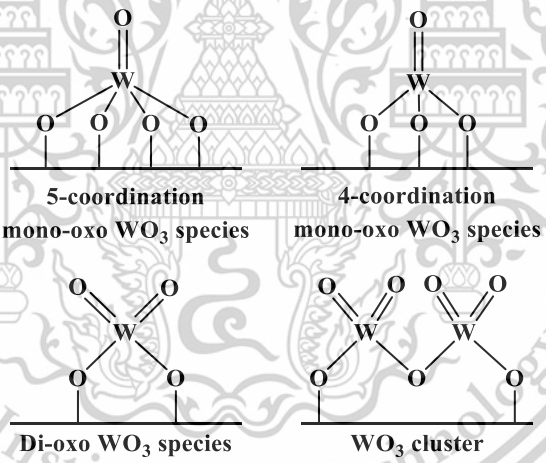

Figure 2.4 Type of WO_3 species.

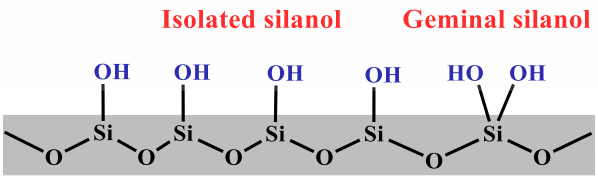

Figure 2.5 Type of surface silanols.

To enhance the formation of single-site WO_3 species, the vicinal and terminal silanols (**Figure 2.5**) would be required. However, the silanols in the amorphous silica

cannot really be controlled. Alternatively, the Copper phyllosilicate (CuPS) – a layered silicate - provided a very high Cu dispersion with only ~3.60 nm (**Figure 2.6**) after the reduction at 250 °C for 2h even at 20wt.% Cu loading [29]. Such high Cu dispersion is attributed to a strong interaction between Cu^{2+} and SiO_2 in the well-defined lamellar structure (**Scheme 2.1**). This could lead to the opportunity to generate the high-concentration region of the vicinal and terminal silanols after leaching the Cu particles. The leaching of Cu is readily under 1.0 M HCl at 40 °C for 1h condition [57].

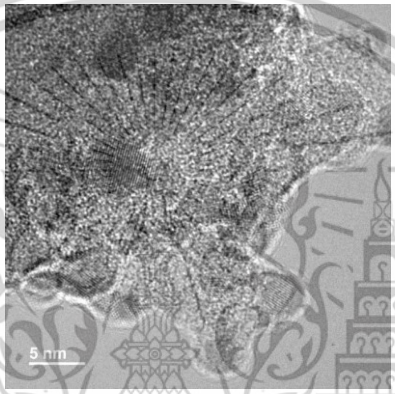

Figure 2.6 TEM images of 20CuPS [29].

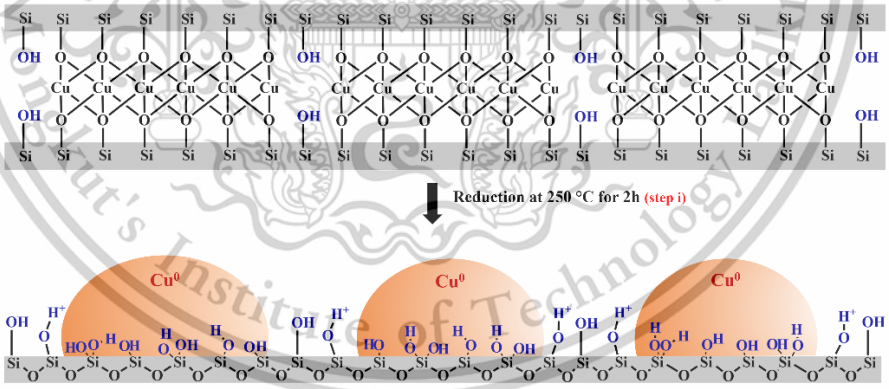

Scheme 2.1 Structure of CuPS.

CHAPTER 3

Research methodology

3.1 Chemicals

The chemicals and substrates used in this research are shown in **Table 3.1.**

Table 3.1. A list of chemicals

Chemicals	Grade of purity	Supplier
Copper (II) nitrate trihydrate	99%	CARLO ERBA
LUDOX® AS-40 colloidal silica	-	SIGMA-ALDRICH
Ammonia solution	30%	CARLO ERBA
Ammonium metatungstate hydrate	100%	SIGMA-ALDRICH
Hydrochloric acid	37%	CARLO ERBA
Fumed Silica (HL-150)	-	Guangzhou GBS High-Tech & Industry
Deionized water	-	-
Air zero gas	99.99%	PRAXAIR
Hydrogen gas	99.99%	PRAXAIR
Nitrogen gas	99.99%	PRAXAIR
Ethylene	99.99%	Labgaz
1% Acetylene/Ethylene		LINDE

3.2 Instruments and apparatus

1. Laboratory glassware
2. Pipette and red bulb
3. Protector laboratory hood, Science Technology
4. Mass flow controller, BROOKS INSTRUMENT LLC, Model SLAS350SB1AB1B2A1D3NAAA
5. Sieve, AASHO N-92, U.S.A standard sieve
6. Quartz wool
7. Quartz tube
8. Universal Indicator

9. Hotplate
10. Hot air oven, UMS00, Memmert
11. Tube furnace with a programmed temperature controller, VCTF4, Vecstar
12. Digital Round-Top Stirring Hot Plate, 3810001, IKA
13. Thermal conductivity detector (TCD), VICI, Valco instrument)
14. Gas chromatography, Shimadzu GC-2010
15. Autoclave

3.3 Catalyst Preparation

3.3.1 Preparation of Copper Phyllosilicate Catalysts (20CuPS and 30CuPS).

Copper phyllosilicates (CuPS) with Cu loadings of 20 wt.% and 30 wt.% were synthesized via the ammonia evaporation hydrothermal method (AHM) [29]. First, the appropriate amounts of copper(II) nitrate trihydrate ($Cu(NO_3)_2{\cdot}3H_2O$) were dissolved in 30 mL of deionized water. Then, four equivalent moles of 30wt.% ammonia aqueous solution was added dropwise to the solution under vigorous stirring. After 30 min, 11.30 mL of colloidal silica was added to the mixture and continuously stirred for 24 h. Then, the mixture was heated at 80 °C in the water bath to evaporate excess ammonia from the solution until pH descended to 7 (from 11). The remaining mixture was transferred to a Teflon line stainless steel autoclaved and hydrothermal treated at 150 °C for 24 h. After that, a precipitate was filtered, washed thrice with deionized water 100 mL, and dried at 60 °C for 24 h in an oven. The obtained powder was then calcined at 400 °C in air (60 mL/min) with a heating rate of 1 °C/min for 4 h. The CuPS corresponding to 20 and 30 wt.% of Cu loading was denoted as 20CuPS and 30CuPS.

Preparation of silanol-rich silica supports from 20CuPS and 30CuPS was proceeded by the Cu leaching of 20CuPS and 30CuPS using 1 M HCl solution. Briefly, 5 g of 20CuPS or 30CuPS was first reduced in a horizontal furnace under H_2 (60 mL/min) at 250 °C for 2 h. Then, 100 mL of 1 M HCl solution was added to the reduced sample and stirred at 60 °C for 1 h. After the filtration, the obtained solids were washed with deionized water until the pH = 7 and dried at 60 °C 24 h in an oven. The samples were denoted as 20CuPS-Le and 30CuPS-Le using 20CuPS and 30CuPS as a precursor, respectively.

3.3.2 Preparation of tungsten over fumed SiO_2 and Le-CuPS supports (5, and 8 %) by incipient wetness impregnation method.

The catalysts were prepared with 5 and 8 % tungsten oxide on fumed silica and Le-CuPS supports. Ammonium metatungstate hydrate was used as a precursor. 5 g of the supports were slowly impregnated by the solution dissolving 0.2786 and 0.7184 g of the tungsten oxide precursor in 7 mL of Deionized water. The impregnated sample was dried at 60 ºC for 24 h and calcined at 550 ºC for 5 h with the flow of air-zero at 60 mL/min.

3.4 Catalyst characterization

3.4.1 Wavelength Dispersive X-ray fluorescence spectrophotometer (WD-XRF).

0.1 g of sample powder was mixed and ground in 4.9 g of boric acid before putting in an Al_2O_3 cup. Subsequently, the number of elements in the sample was measured by a Wavelength Dispersive X-ray fluorescence spectrophotometer, Rigaku (25X PrimusIV) using CuK_α radiation (λ = 1.504056 Å).

3.4.2 X-ray diffractometry (XRD)

The crystallinity and structural characteristics of the catalysts were identified by X-ray diffraction spectrophotometer, DMAX2200 Ultima+ (Rigaku) diffractometer by Cu K_α radiation (λ = 1.504056 Å). Each sample was tightly packed into an aluminum holder and positioned at the center of the height reference sample plate under ambient air conditions. The data was collected at Bragg angle (2θ) from 5˚ to 80˚ with a scanning rate of 50°. min^{1}.

3.4.3 Surface area measurement

N_2 adsorption-desorption isotherms were recorded by the TOP200 (Altamira Instruments) instrument and evaluated with a partial pressure (P/P_0) range of 10^{-6} to 1.0. Briefly, 50 mg of the samples were evacuated at 300 ºC for 12 h under vacuum, and the nitrogen was subjected at -195 ºC for the N_2 adsorption-desorption experiment. The samples's specific surface area was calculated using the BET and BJH methods, respectively.

3.4.4 Diffuse reflectance UV-VIS spectrophotometer (DR UV-Vis)

Diffuse reflectance UV-Vis (DR-UV) spectra were obtained using a UV-Vis spectrometer (T92+, PG Instruments). Briefly, the samples were mixed with $BaSO_4$,

pressed into a sample holder, and covered with a quartz slide. Spectral data were recorded over a wavelength range of 200 to 800 nm, using $BaSO_4$ as the baseline reference. All measurements were conducted under ambient conditions.

3.4.5 Raman spectroscopy

Raman spectra were acquired using Raman spectrometers (Nanoproton and Ramantouch Force) with a 785 nm laser. The laser excitation power was set to 6.11 mW, with an exposure time of 100 s. Spectra were collected over a range of 0 to 2000 cm^{-1}, using a silicon (Si) standard. All samples were prepared under ambient conditions for Raman analysis.

3.4.6 Solid-state ^{29}Si Cross-Polarization Magic Angle Spinning Nuclear Magnetic Resonance (^{29}Si CPMAS NMR)

Solid-state ^{29}Si CPMAS NMR spectra were recorded using a JEOL Resonance JNM-ECZ400R/S1 spectrometer (400 MHz). The experiments were conducted using a 4 mm double-resonance MAS probe, operating at a spinning speed of 10 kHz. The acquisition parameters included a contact time of 2 ms, a relaxation delay of 5 s, and a 90° pulse width of 3.192 µs. Proton decoupling was performed using the Two-Pulse Phase Modulation (TPPM) scheme at room temperature under ambient conditions, with a total of 2160 scans collected. NMR data were processed using Delta software, employing Fourier transform (FT) with phase and baseline correction. The detailed parameters are listed in ESI. The spectra were subsequently deconvoluted using Gaussians to determine the relative proportions of Q_2, Q_3, and Q_4 silicate species. The sample was carefully packed into the rotor in a known quantity, ensuring measurement consistency. To establish a calibration curve for surface silanol quantification, silicic acid (8–25 mg) was used as a standard reference.

3.4.7 Inductively Coupled Plasma Optical Emission spectroscopy (ICP-OES)

ICP-OES analysis was performed by ICP-OES Analyzers, Avio 500 Max (PerkinElmer). The samples were digested using graphite block acid digestion system, ECO-PRE, ODLAB. Briefly, ~0.1 g of sample and the mixture of 30 mL H_2SO_4 and 15 mL HNO_3 were mixed in a PTFE vessel. Subsequently, the mixture was heated at 210 °C for 12 h with a heating rate of 2 °C/min, filtered, and dissolved in deionized water

3.4.8 Scanning Electron Microscope (SEM)

SEM micrographs of catalysts were obtained with a FEI (Quanta 250 model) for determining the size of crystalline and morphology, using an ETD detector and

accelerating voltage of 15 kV. The samples were first sonicated in acetone and then dispersed onto a glass slide. A piece of carbon tape was mounted on a specimen stub and placed onto the dispersed sample for imaging.

3.4.9 Extended X-ray Absorption Fine Structure (EXAFS)

EXAFS measurements were performed at beamlines 5.2 and 8 XAS of the Synchrotron Light Research Institute (SLRI), Thailand. W L_3-edge XANES and EXAFS spectra were measured in transmission mode using the two-ionization chamber. The Ge (220) double crystal monochromator was used to scan photon energy in 0.3 eV increments. The k2-weight spectra were Fourier transformed within the k-range of 3 and 10 for all elements, where k denotes the wave vector. Energy calibration was carried out using W foil (L_3-edge) standard at 10,209.9 eV. The samples were finely ground and mixed using an agate mortar, then pressed into a polypropylene frame (1.5 cm x 0.6 cm slit width) mounted on Kapton tape (polyimide) under ambient condition. The assembly was sealed with polypropylene film and placed inside the vacuum chamber. The spectra were normalized, processed, and analyzed on Athena software.

3.5 Catalytic activity testing

Cross-metathesis reaction was performed in a continuous fixed-bed reactor operated (**Figure 3.1**) under atmospheric pressure. Before the catalytic testing, the catalyst (50mg) was placed into a middle of 8 mm diameter quartz tube (bed height of 15 mm) and covered with quartz wool, and supported by quartz beads at the bottom. The reactor was located at the center of a vertical tube furnace. The catalysts were activated at 500°C with a heating rate of 10 °C/min for 2 h under air-zero at a flow rate of 30 mL/min. Subsequently, the temperature increased to 600 °C under a N_2 atmosphere at the same heating rate. The catalysts were then subjected to ethylene treatment (99.9%, 30 mL/min) at 600 °C for 2 hours. The ethylene pretreatment conditions were based on optimization data reported in a previous study [25]. The reaction was operated at 450°C and a feed gas containing 1% v/v acetylene in ethylene, delivered at a flow rate of 20 mL/min with N_2 35 mL/min as carrier gas. The gas products were periodically sampled every 30 minutes over a 5-hour period using an online GC (Shimadzu 2010).

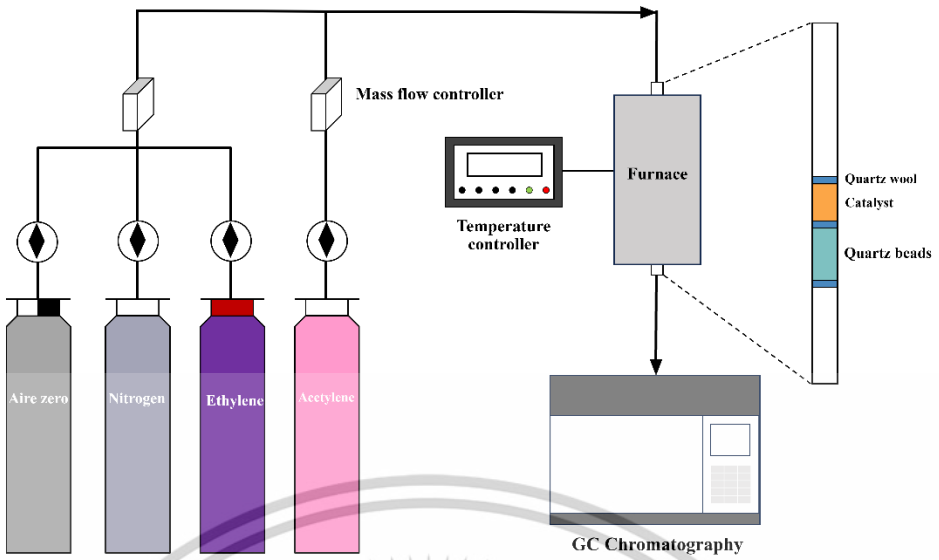

Figure 3.1 Schematic diagram of the catalytic testing rig.

The gas product was quantified by GC-FID equipped with Al_2O_3 plot column. The operating condition of gas chromatography is shown in **Table 3.2.**

Table 3.2 Operating condition of gas chromatography.

Gas Chromatography	Condition
Carrier gas	N_2
Carrier gas flow rate (mL/min)	5
Injection temperature (°C)	250
Detector temperature (°C)	300
Initial column temperature (°C)	40
Final column temperature (°C)	180

Chapter 4
Main results and Discussion

4.1 Physicochemical properties of CuPS as a support template

The layered phyllosilicate structure of 20CuPS and 30CuPS was confirmed by XRD analysis, as depicted in **Figure 4.1a-b**. The diffraction peaks observed at 30.8˚, 35.0˚, 57.6˚, and 63.4˚ were assigned to the chrysocolla phase ($Cu_2Si_2O_5(OH)_2$), consistent with the copper phyllosilicate structure those reported in the literature [30,58–60]. The Cu content in 20CuPS and 30CuPS aligned well with the expected values (**Table 4.1**, entries 1–2). Due to the layered structure of the phyllosilicates, these samples exhibited significantly higher surface areas (>344 m^2/g) compared to fumed SiO_2 (150 m^2/g).

Furthermore, an increase in Cu loading led to a surface area enhancement, rising from 344 m^2/g for 20CuPS to 400 m^2/g for 30CuPS. Moreover, 20CuPS exhibited a slightly larger pore volume (1.35 cm^3/g) than 30CuPS (1.21 cm^3/g). This reduction in pore volume at higher Cu loading is likely due to the increased formation of chrysocolla structures, which require Cu_{2+} ions to bridge tetrahedral silica layers via octahedral coordination sites ($Cu^{2+}(OSi)_6$), as shown in **Scheme 4.1**. The strong interconnection between Cuo_6 octahedra and SiO_4 tetrahedra, driven by high charge density, resulted in a more compact lamellar structure, thereby decreasing the pore volume. Consistently, the amorphous silica peak at ~20° (**Figure 4.1b**) was less pronounced in 30CuPS, correlating with its higher surface area.

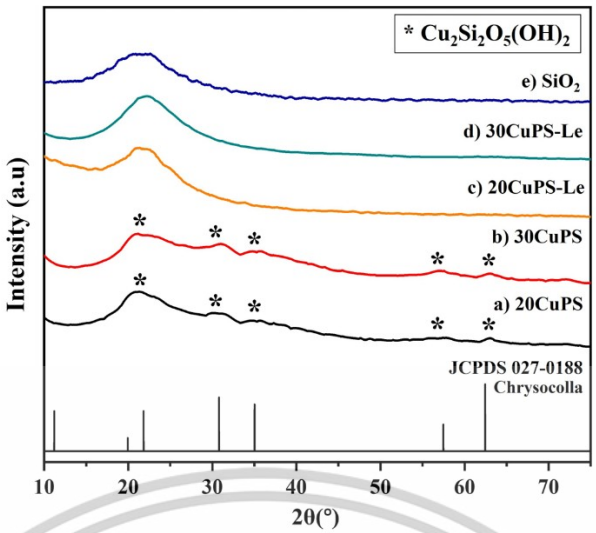

Figure 4.1 Comparison of XRD spectra for CuPS, Cu-leached CuPS, and fumed silica (SiO_2).

Table 4.1 Physical and Chemical properties of CuPS and Cu-leached CuPS samples compared with fumed SiO_2.

Entry	Sample	Cu loading (wt.%)[a]	N_2 adsorption-desorption		
			S_{BET} (m^2/g)[c]	d_p (nm)[c]	V_p (cm^3/g)[c]
1	20CuPS-cal	19.3	344	15.8	1.35
2	30CuPS-cal	28.8	400	12.1	1.21
3	20CuPS-red	19.3	183	12.6	0.58
4	30CuPS-red	28.8	230	9.8	0.56
5	20CuPS-Le	0.06	191	25.9	1.24
6	30CuPS-Le	0.04	383	18.8	1.10
7	SiO_2	-	150	22.7	0.54

[a]Determined by ICP-OES, [b]Determined by Multipoint BET.

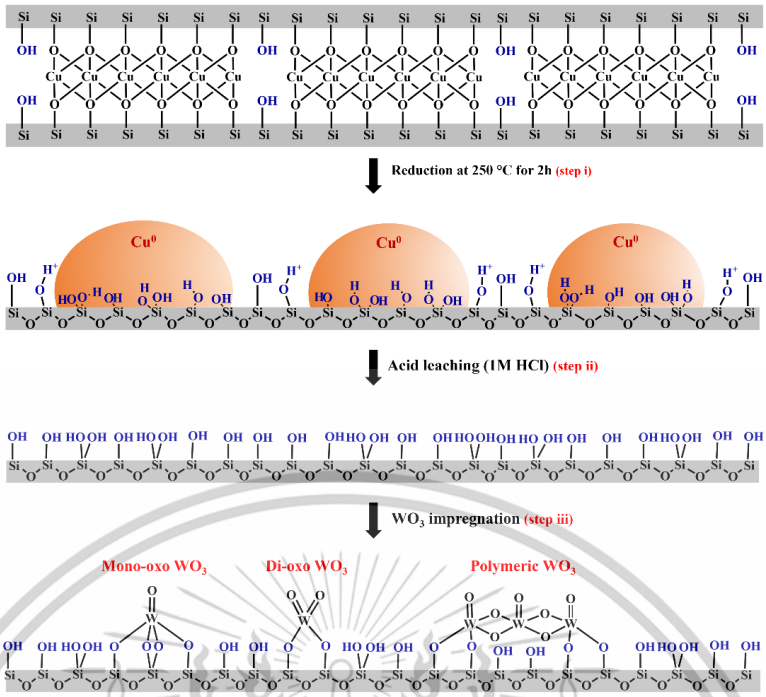

Scheme 4.1 Development of silanol-enriched SiO_2 and surface WO_3 species on Cu-leached CuPS supports.

Copper was effectively removed from 20CuPS and 30CuPS following the leaching process, as evidenced by ICP-OES analysis, which detected only trace amounts of Cu (<0.06 wt.%) in 20CuPS-Le and 30CuPS-Le (**Table 4.1**, entries 5-6). The absence of diffraction peaks associated with chrysocolla in the XRD patterns of the Cu-leached samples (**Figure 4.1c-d**). Instead, a prominent amorphous SiO_2 peak at ~23° was detected in both 20CuPS-Le and 30CuPS-Le, resembling the pattern of fumed SiO_2. This outcome can be attributed to the reduction process (250 °C under H_2 for 2 h), which yielded fine Cu particles (<5 nm) from 20CuPS and 30CuPS (**Scheme 4.1**, step i) [61,62]. The leaching of these small Cu particles using 1 M HCl at 60 °C proved to be more efficient compared to the calcined CuPS samples, where no Cu^{2+} was removed under the same conditions due to the strong Cu^{2+}-SiO_2 interactions in octahedral sites. The structural collapse induced by reduction, as evidenced by XRD (**Figure 4.2**), also resulted in decreased surface area and pore volume (183–230 m²/g, 0.56–0.58 cm³/g; **Table 4.1**, entries 3–4), leading to weaker metal–support interactions. Consequently, Cu leaching was facilitated through the exposure of surface silanol groups derived from Si–O–Cu–O–Si linkages (**Scheme 4.1**, step ii) [29,63].

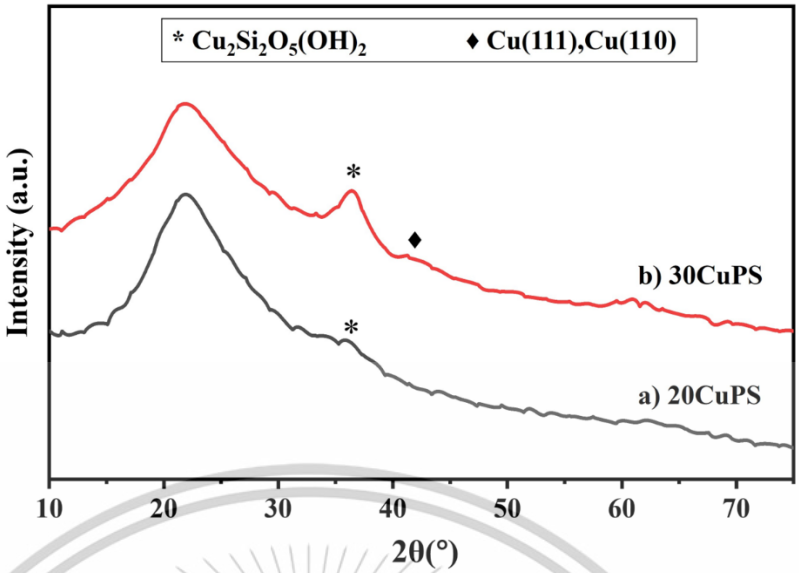

Figure 4.2 Comparison of XRD spectra for reduced i) 20CuPS and ii) 30CuPS.

Nevertheless, the Cu-leached CuPS samples (20CuPS-Le and 30CuPS-Le) exhibited a higher surface area, larger pore volume, and pore diameter (191-383 m^2/g, 1.10-1.24 cm^3/g, 18.8-25.9 nm, **Table 4.1**, entries 5-6) compared to the reduced samples. Since leaching was conducted in an acidic solution at a relatively low temperature, condensation/dehydroxylation of the exposed silanol group was avoided (**Scheme 4.1**), preserving the overall particle size and morphology. The increased surface area and porosity observed in the Cu-leached samples suggest the formation of structural defects and silanol groups at the sites of Cu dissolution. Therefore, the removal of Cu particles could provide additional accessible pores, resulting in a higher surface area than fumed silica (150 m^2/g, **Table 4.1**, entry 7). In addition to the increased surface area, a higher amount of silanols can be observed for 20CuPS-Le and 30CuPS-Le. ^{29}Si CPMAS NMR spectra, recorded with similar sample amounts (~30 mg), revealed a more intense Si-OH signal at approximately –100 ppm compared to fumed SiO_2 (**Figure 4.3a**). Given that ^{29}Si CPMAS NMR detects signals based on cross-polarization between H and Si, the observed ^{29}Si signal originates from ^{29}Si atoms in close proximity to OH groups. Therefore, the signal intensity of Q_2 (-90 ppm, geminal silanol, Si-(O-H)$_2$) and Q_3 (-100 ppm, isolated silanol, Si-OH) proportionally indicate the relative amounts of surface silanols [64–66]. Meanwhile, the signal of Q_4 (-110 ppm, siloxane, Si-(OSi)$_4$) was less pronounced.

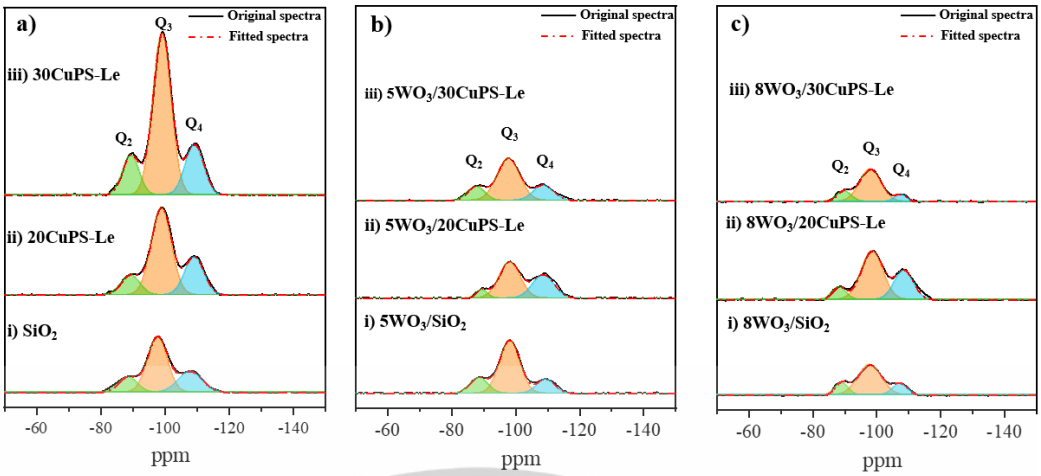

Figure 4.3 ^{29}Si CPMAS NMR spectra of a) parent siliceous supports, b) 5wt.% WO_3 over various siliceous supports, and c) 8wt.% WO_3 over various siliceous supports.

The signal intensities of Q_2 and Q_3, which equivalently represent surface silanols, can be utilized to quantify the number of surface silanols using a calibration curve derived from a silicic acid standard (4.07 mmol OH/g, **Figure 4.4**). As shown in **Table 4.3**, the number of surface silanols increases in the order of fumed SiO_2 < 20CuPS-Le < 30CuPS-Le (**Table 4.2**). However, the density of OH groups per nm² remains relatively consistent across these materials, indicating that the total number of surface silanols is primarily dependent on the surface area (**Table 4.1**).

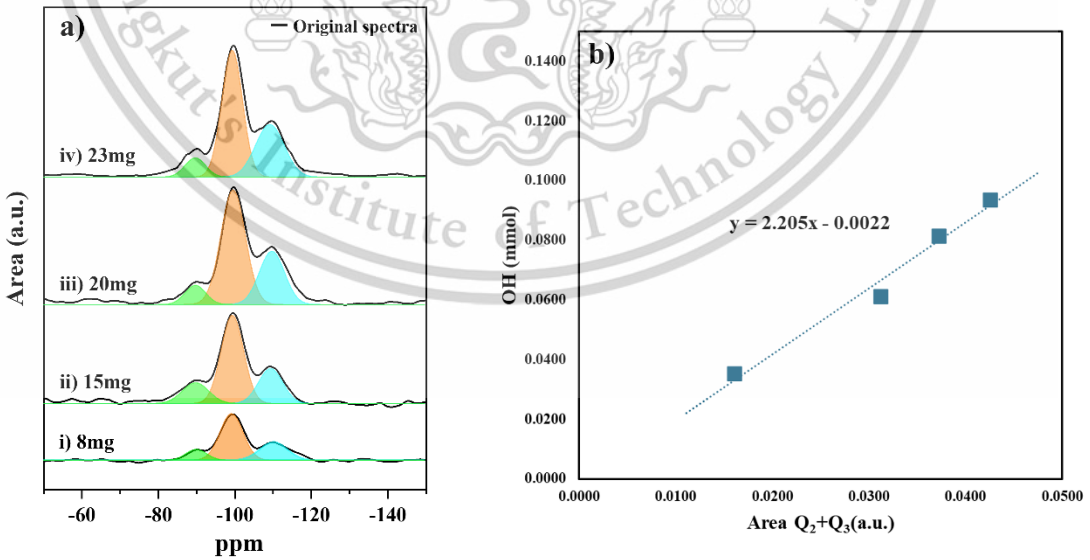

Figure 4.4 a) ^{29}Si CPMAS NMR spectra of silicic acid and b) the calibration curve.

Table 4.2 Surface silanols calculated from deconvolution of ^{29}Si CPMAS NMR spectra using Gaussian.

Entry	Samples	Integral area (a.u.)			Surface Si-OH (mmol OH/g)			Fraction (%)	
		Q_2 (-90)	Q_3 (-100)	Total	Q_2 (-90)	Q_3 (-100)	Total	Q_2	Q_3
1	SiO_2	0.0046	0.0171	0.0217	0.31	1.37	1.76	21.19	78.80
2	$5WO_3/SiO_2$	0.0045	0.0172	0.0217	0.21	0.99	1.27	20.74	79.26
3	$8WO_3/SiO_2$	0.0026	0.0114	0.0140	0.09	0.57	0.72	18.57	81.43
4	20CuPS-Le	0.0058	0.0275	0.0333	0.38	2.09	2.54	17.42	82.58
5	$5WO_3$/20CuPS-Le	0.0028	0.0169	0.0197	0.10	0.90	1.06	14.21	85.79
6	$8WO_3$/20CuPS-Le	0.0015	0.0123	0.0138	0.03	0.62	0.71	10.87	89.13
7	30CuPS-Le	0.0140	0.0466	0.0606	0.96	3.35	4.38	23.10	76.90
8	$5WO_3$/30CuPS-Le	0.0038	0.0154	0.0192	0.19	0.99	1.25	19.79	80.21
9	$8WO_3$/30CuPS-Le	0.0025	0.0110	0.0135	0.11	0.74	0.92	18.52	81.48

Table 4.3 Density of surface silanol groups on siliceous supports.

Entry	Sample	Q_2 (a.u.)	Q_3 (a.u.)	Geminal Si-OH (mmol OH/g)	Isolated Si-OH (mmol OH/g)	Total surface Si-OH (mmol OH/g)	Surface Si-OH density (OH/nm^2)
1	SiO_2	0.0046	0.0171	0.3	1.4	1.8	7.0
2	20CuPS-Le	0.0058	0.0275	0.4	2.1	2.5	8.0
3	30CuPS-Le	0.0140	0.0466	1.0	3.4	4.4	6.9

Note: The signal intensity of Q_2 and Q_3 obtained from ^{29}Si CPMAS NMR spectra and the surface silanols, determined by the number of surface silanols based on a calibration curve of silicic acid (4.07 mmol OH/g) standard in ***Figure 4.4****.*

In addition to surface area, the amount of silanol plays a crucial role in WO_3 accommodation. The isolated silanols ($(Si\text{-}O)_3$ Si-OH, Q_3, −100 ppm) were predominant in the Cu-leached CuPS samples (~80%, 2–3 mmol OH/g, **Table 4.2**), while geminal silanols ($(Si\text{-}(O\text{-}H)_2$, Q_2, −90 ppm) were relatively less abundant (~20%, 0.5–1.0 mmol OH/g). This suggests that following Cu leaching, the remaining silica surface is largely terminated by isolated silanols. Moreover, the concentrations of both isolated and geminal silanols increased significantly in 20CuPS-Le (1.5-fold) and 30CuPS-Le (2.8-fold) compared to fumed SiO_2 (**Table 4.2**). This increase is attributed

to the higher Cu loading in CuPS, which provides a greater number of Cu^{2+} octahedral sites ($Cu^{2+}(OSi)_6$) embedded within the tetrahedral silica layer, as indicated by the XRD pattern and **Scheme 4.1**. Consequently, Cu leaching results in a higher density of isolated silanols, particularly in 30CuPS-Le. Additionally, SEM analysis (**Figure 4.5**) revealed that the Cu-leached CuPS samples exhibit a more uniform spherical morphology, whereas fumed SiO_2 consists of aggregated particles. The reduced particle agglomeration in the Cu-leached samples likely enhances the accessibility of surface silanols, thereby improving the dispersion of WO_3. As a result, the silanol-rich silica obtained from the CuPS precursor offers high-loading and well-dispersed WO_3 species.

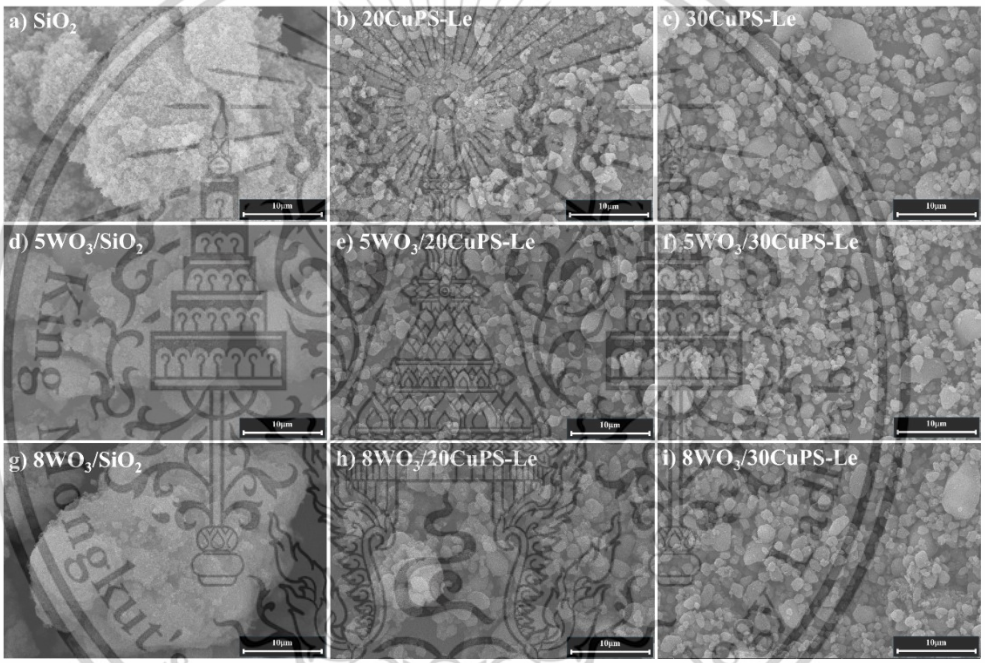

Figure 4.5. SEM images of supports and WO_3 supported catalysts.

4.2 WO_3 over silanol-rich supports from CuPS-Le

Following the incorporation of 5wt.% WO_3 onto 20CuPS-Le and 30CuPS-Le, a substantial reduction in the silanol signal was observed (**Figure 4.3b**). Correspondingly, the surface area of 5wt.% WO_3supported catalysts decreased (**Table 4.4**) relative to their parent materials (**Table 4.1**). Notably, SEM analysis revealed no evidence of particle agglomeration or surface topology modifications (**Figure 4.5**), suggesting that the loaded WO_3 was anchored to the exposed surface silanols via Si–O–W bonds (**Scheme 4.1**, step iii), resulting in highly dispersed WO_3 species, such as single-site and polymeric species [27,67,68]. In line with this view, the XRD pattern

of $5WO_3$/20CuPS-Le, $5WO_3$/30CuPS-Le, and $5WO_3/SiO_2$ showed the absence of bulk WO_3 phases, with only an amorphous SiO_2 reflection at ~23° (**Figure 4.6a**). In a supportive manner, the W L_3-edge energy (10,209.5 eV, **Table 4.4**, **Figure 4.6d**), DR-UV spectra (**Figure 4.6b**), and band gap energy (Eg) of ~3.7-4.1 eV, calculated using the Tauc plot (**Table 4.4**, **Figures 4.7a-c**), were consistent across $5WO_3$/20CuPS-Le, $5WO_3$/30CuPS-Le, and $5WO_3/SiO_2$, further confirming the presence of single-site and/or polymeric WO_3 species [69,70]. were obtained from $5WO_3$/20CuPS-Le, $5WO_3$/30CuPS-Le, and $5WO_3/SiO_2$.

In addition to this point, the EXAFS spectra of $5WO_3$/20CuPS-Le, $5WO_3$/30CuPS-Le, and $5WO_3/SiO_2$ exhibited similar features (**Figure 4.6c**). The higher intensity of the first coordination shell at distance R(W–O) ∼ 1.3 Å and a lower second-shell peak at distance R(W–O) ∼ 2.0 Å, characteristic of WO_6 octahedral further confirmed the absence of bulk WO_3 and the presence of highly dispersed WO_3 species [71–73]. Hence, the XRD patterns, DR-UV, and EXAFS results indicate that all supported WO_3 catalysts contain similarly dispersed WO_3 species, likely due to excessive silanol sites available to accommodate the 5 wt.% WO_3 loading.

Table 4.4 Physical and chemical properties of supported WO_3 catalysts.

Entry	Sample	WO_3 loading (wt.%)[a]	N_2 adsorption-desorption			Band Gap (eV)[c]	Energy edge (eV)[d]
			S_{BET} (m^2/g)[b]	d_p (nm)[b]	V_p (cm^3/g)[b]		
1	$5WO_3/SiO_2$	4.5	146	30.5	0.99	3.88, 4.09	10209.5
2	$5WO_3$/20CuPS-Le	4.7	192	24.3	1.15	3.81	10209.5
3	$5WO_3$/30CuPS-Le	5.1	306	15.2	1.09	3.79	10209.5
4	$8WO_3/SiO_2$	7.8	141	32.4	0.82	2.94	10209.5
5	$8WO_3$/20CuPS-Le	8.1	180	21.6	0.92	3.36	10209.5
6	$8WO_3$/30CuPS-Le	7.9	282	19.1	1.05	3.71	10209.5

*[a]Determined by XRF, [b]Determined by Multipoint BET, [c]Determined by DR-UV, [d] Determined by W L_3 XANES (**Figure 4.6d**).*

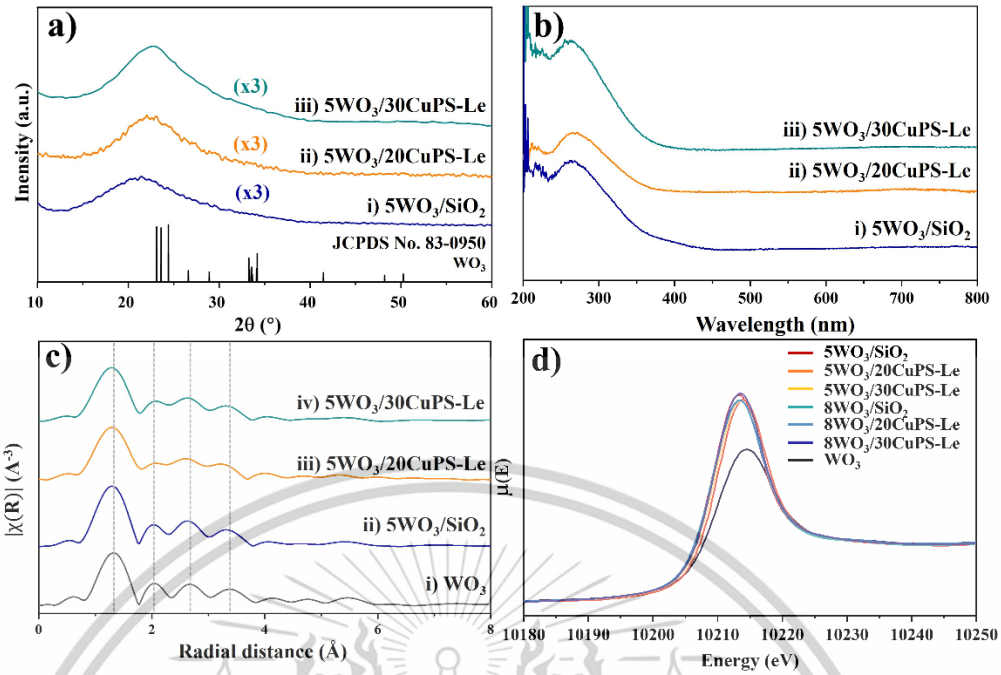

Figure 4.6 a) XRD patterns, b) DR-UV spectra, c) W L_3-edge EXAFS spectra of 5wt.% WO_3 loading over siliceous supports and d) W L_3-edge XANES spectra of supported WO_3 catalysts and bulk WO_3.

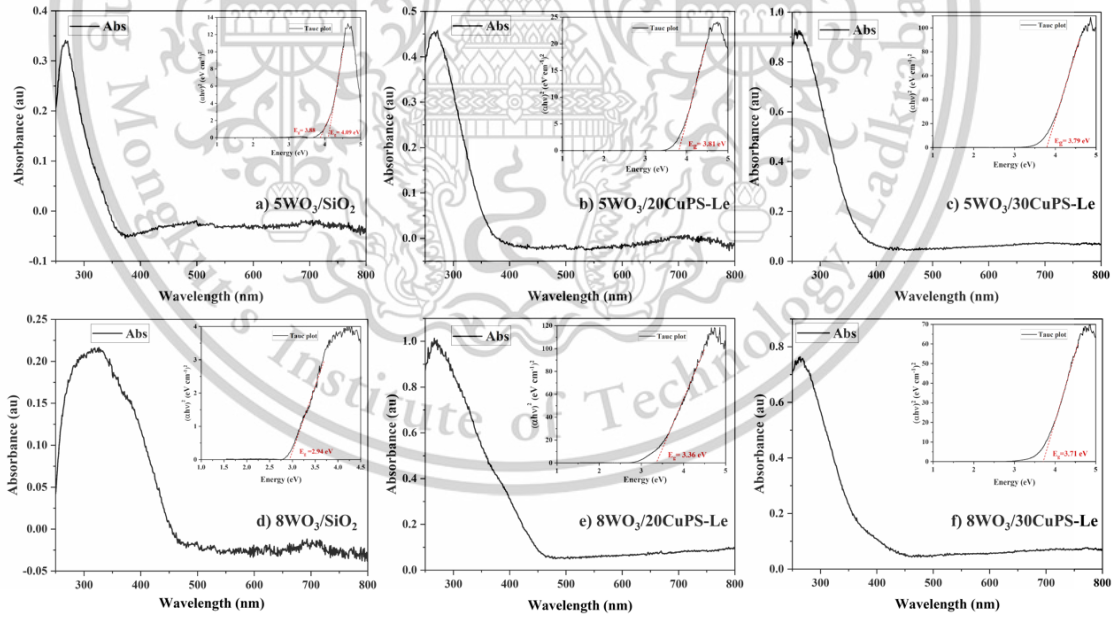

Figure 4.7. DR-UV absorption spectra and Tauc plot (Insert picture) of supported WO_3 catalysts.

Since the highly dispersed WO_3 species can be accommodated by the available silanols on all supports, similar catalytic activity (~57-60% conversion, TOF = ~28-30 h^{-1}) for 1,3-butadiene production via the cross-metathesis of

acetylene-ethylene was observed across the supported 5wt.% WO_3 catalysts (**Table 4.5**, entries 1-3). This could be ascribed to the presence of highly dispersed WO_3 species, i.e., single-site and polymeric are effectively in $5WO_3$/30CuPS-Le, $5WO_3$/20CuPS-Le, and $5WO_3/SiO_2$, as previously discussed. Furthermore, the adjacent silanol groups are critical in facilitating active site formation for olefin metathesis. These silanols enable tungsten reduction, stabilizing key reaction intermediates, and assisting in hydrogen transfers that lead to forming active W(VI) alkylidene species [74]. All catalysts exhibited high selectivity (~74%) toward 1,3-butadiene, with a production rate of 4.6-4.8 $mmol_{1,3\text{-butadiene}}/h{\cdot}g_{cat}$. Additionally, cyclohexene and benzene were observed as minor products, consistent with the well-known secondary Diels–Alder reaction between 1,3-butadiene and ethylene, forming cyclohexene, which subsequently undergoes dehydrogenation to benzene (**Scheme 4.2**) [25,39,75]. Notably, all catalysts demonstrated stable performance over time, as shown in **Figure 4.8**.

Table 4.5 Acetylene/ethylene cross-metathesis over WO_3 supported on siliceous supports.

Entry	Catalysts	Acetylene Conversion (%)	Activity ($mmol_{feed}/h{\cdot}g_{cat}$)	1,3-butadiene production rate ($mmol/h{\cdot}g_{cat}$)	Yield (%)			Selectivity (%)			Mass balance (%)
					1,3-Butadiene	Cyclohexene	Benzene	1,3-Butadiene	Cyclohexene	Benzene	
1	$5WO_3/SiO_2$	57	6.1	4.6	43	9	8	75	15	14	102
2	$5WO_3$/20CuPS-Le	60	6.4	4.7	44	5	8	73	8	13	95
3	$5WO_3$/30CuPS-Le	61	6.5	4.8	45	8	9	74	13	14	101
4	$8WO_3/SiO_2$	37	4.0	2.5	23	3	5	62	8	13	84
5	$8WO_3$/20CuPS-Le	65	7.0	5.1	48	6	8	74	9	12	94
6	$8WO_3$/30CuPS-Le	72	7.7	6.3	59	8	8	82	11	11	105

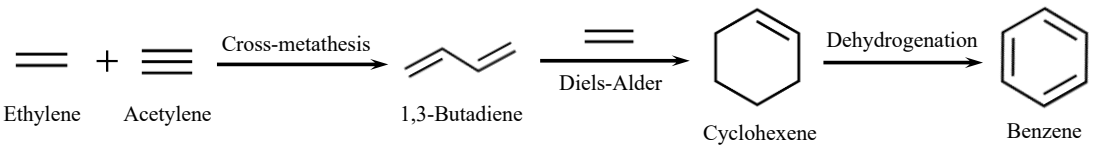

Scheme 4.2 Cross-metathesis of acetylene/ethylene and Diels-Alder reaction.

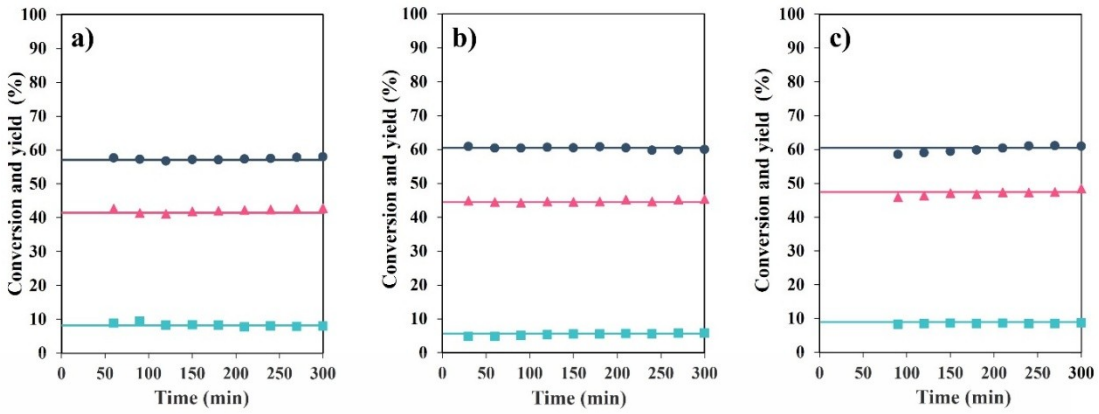

Figure 4.8 Reaction time profile for cross-metathesis of acetylene/ethylene using a) $5WO_3/SiO_2$, b) $5WO_3$/20CuPS-Le and c) $5WO_3$/30CuPS-Le; (●) conversion, (▲) 1,3-butadiene, (■) cyclohexene.

Despite the higher WO_3 loading, a significant decrease in cross-metathesis activity was observed for $8WO_3/SiO_2$. This catalyst exhibited only 37% conversion (4.0 $mmol_{feed}/h{\cdot}g_{cat}$) with a 1,3-butadiene production rate of 2.5 mmol /$h{\cdot}g_{cat}$ (**Table 4.5**, entry 4), compared to 57% conversion (6.1 $mmol_{feed}/h{\cdot}g_{cat}$) and 4.6 $mmol_{1,3\text{-butadiene}}/h{\cdot}g_{cat}$ for $5WO_3/SiO_2$ (**Table 4.5**, entry 1). The activity reduction can be attributed to the formation of bulk WO_3 in $8WO_3/SiO_2$, as evidenced by the presence of crystalline m-WO_3 in the XRD pattern (**Figure 4.9a**, i). In addition, the confirmation of bulk WO_3 formation was confirmed by the broad DR-UV peak in the range of 250–450 nm (**Figure 4.9b**, i) and the corresponding E_g band for typical bulk WO_3 (~2.9 eV) (**Table 4.4**, entry 4; **Figure 4.7d**) [54,70]. Raman spectra (**Figure 4.10a**, i) show characteristic peaks at 268 cm^{-1} (δ(W=O)) and 711 and 804 cm^{-1} (υ(W-O-W)), further supporting bulk WO_3 formation [27,76–78]. In line with this view, EXAFS spectra indicate the presence of polymeric and bulk WO_3 species, with a W–W radial distance of ~3.4 Å (**Figure 4.10b**, i) [71,72]. These findings suggest that the increased WO_3 loading in $8WO_3/SiO_2$ led to lower dispersion and the formation of bulk WO_3, consequently reducing the density of active $W{=}CH_2$ species and leading to lower 1,3-butadiene production (**Table 4.5**, entry 4) compared to $5WO_3/SiO_2$ (**Table 4.5**, entry 1).

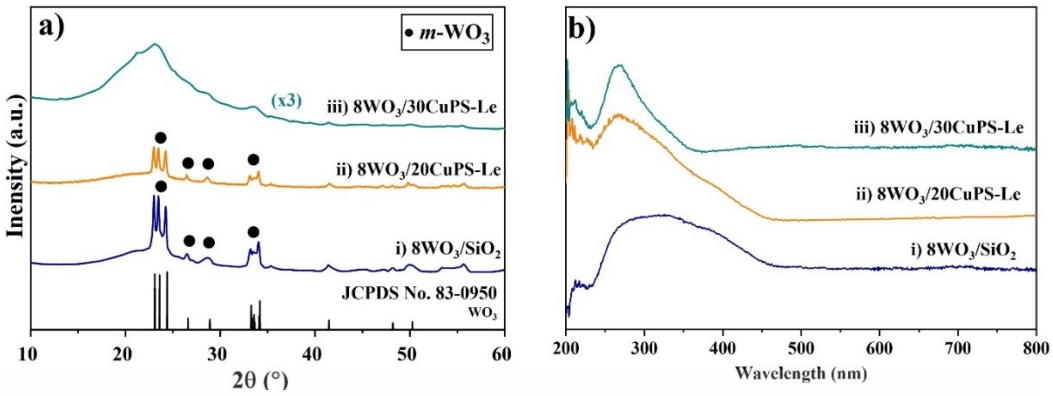

Figure 4.9 a) XRD patterns and b) DR-UV spectra of 8wt.% WO_3 loading over siliceous supports.

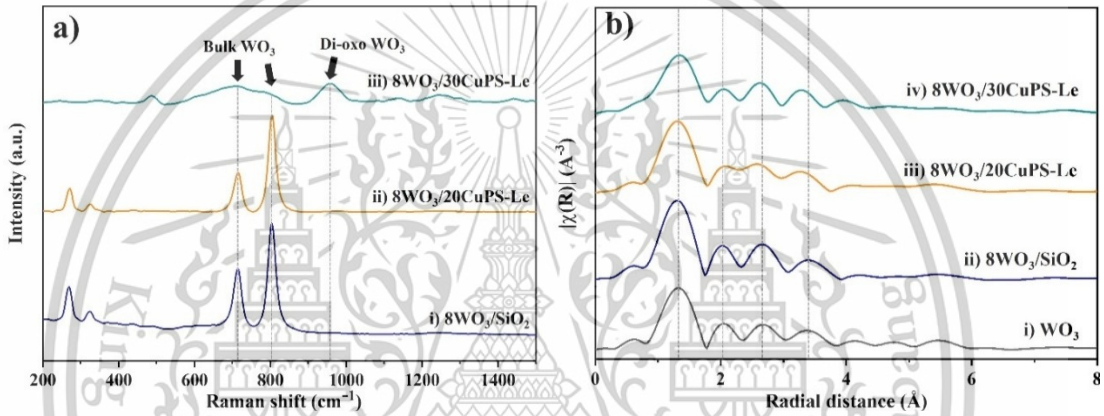

Figure 4.10 a) Raman and b) W L_3-edge EXAFS spectra of 8wt.% WO_3 loading over siliceous supports.

The formation of bulk WO_3 in $8WO_3/SiO_2$ suggests a limited number of isolated and geminal silanols available to interact with incorporated WO_3 at high loading (8 wt.%). This is evidenced by the relatively small fraction of silanols consumed (35%, **Figure 4.3** and **Figure 4.11a**) following WO_3 impregnation. Consequently, only a small portion of WO_3 can directly bond to the surface (Si-O-WO_x), forming highly dispersed species, such as single-site ($(O=)_2W(OSi)_2$, $O=W(OSi)_4$) and polymeric WO_3 ($(W\text{-}O)_x$-W-OSi). Meanwhile the remaining surface silanols weakly interact with WO_3, leading to WO_3 agglomeration at high loading. Additionally, the agglomeration of SiO_2 particles results in reduced accessibility of silanols for WO_3 accommodation. In sharp contrast, a significantly higher fraction of surface silanols were consumed in $8WO_3$/30CuPS-Le (77%, **Figure 4.11a**) compared to $8WO_3/SiO_2$ and $8WO_3$/20CuPS-Le. This suggests that the exposed silanols in 30CuPS-Le effectively accommodate highly dispersed WO_3 species, even at high loading (8 wt.%). Consistent with this observation,

DR-UV analysis revealed no bulk WO_3 formation in $8WO_3$/30CuPS-Le, as confirmed by the absence of crystalline WO_3 peaks in the XRD pattern (**Figure 4.9a**, iii). The band gap energy of $8WO_3$/30CuPS-Le (~3.71 eV, **Table 4.4**, **Figure 4.7f**) was comparable to that of $5WO_3$/30CuPS-Le. The Raman spectrum exhibited a characteristic peak at 970 cm^{-1} (**Figure 4.10a**, iii), confirming the presence of single-site dioxo WO_3 species. In addition, the lower-intensity peaks at 711 and 804 cm^{-1}, associated with bulk WO_3, suggest the presence of small WO_3 clusters [72,76,77,79]. Furthermore, EXAFS analysis of $8WO_3$/30CuPS-Le (**Figure 4.10b**, iv) showed a slightly shorter W–W radial distance (3.27 Å) compared to other samples (~3.4 Å), further indicating the formation of smaller WO_3 clusters [72].

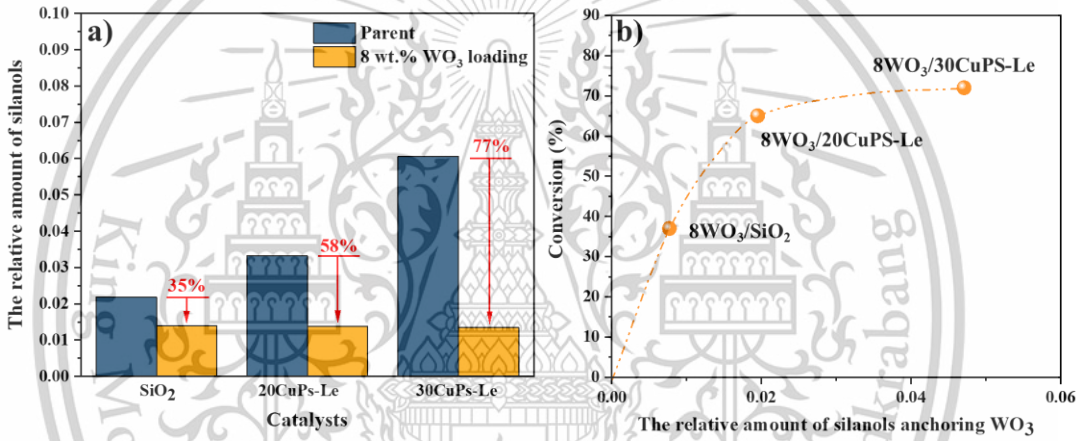

Figure 4.11 a) The decrease in ^{29}Si CPMAS NMR signal intensity and b) the relative amount of silanols anchoring WO_3 and conversion. *The corresponding calculations are provided in Appendix A6-A7.*

The presence of bulk WO_3 in $8WO_3$/20CuPS-Le, as evidenced by XRD, DR-UV, Raman, and EXAFS spectra (**Figures 4.9–4.10**), indicates that the surface silanols in 20CuPS-Le are insufficient to accommodate an 8wt.% WO_3 loading. The lower surface area of 20CuPS-Le probably promotes WO_3 agglomeration due to the close proximity of surface WO_3 species, in contrast to the more dispersed WO_3 observed in $8WO_3$/30CuPS-Le. As a result, $8WO_3$/20CuPS-Le exhibited only a modest increase in conversion from 60% to 65% (**Table 4.5**, entry 5) compared to $5WO_3$/20CuPS-Le (**Table 4.5**, entry 2).

Conversely, the high WO_3 dispersion in $8WO_3$/30CuPS-Le, as discussed earlier, led to a significantly higher acetylene conversion (72%, **Table 4.5**, entry 6) and a

1,3-butadiene production rate of 6.3 mmol/h·g_{cat}, along with excellent stability (**Figure 4.12**). This again emphasized the crucial role of available isolated and geminal silanols in interacting with WO_3 to form highly dispersed WO_3 active species. Thus, the silanol-rich SiO_2 obtained from Cu-leached 30CuPS effectively accommodates 8wt.% WO_3 with high dispersion. Therefore, the acetylene conversion increased proportionally with the amount of silanols that anchor WO_3, as shown in **Figure 4.11b**.

Notably, $8WO_3$/30CuPS-Le exhibited a higher 1,3-butadiene production rate compared to WO_3 catalysts supported on other high-surface-area materials, such as confined mesoporous silica and SiO_2 (Davisil, 4.0 OH/nm², **Figure 4.13**, **Table 4.6**). This highlights the critical role of isolated and geminal silanols in 30CuPS-Le in facilitating WO_3 dispersion and catalytic activity beyond the effect of surface area alone. Although the 1,3-butadiene production rate (6.3 mmol/h·g_{cat}) obtained in this work was lower than that achieved in homogeneous systems (12.5 mmol/h·g_{cat}), the superior selectivity attained with $8WO_3$/30CuPS-Le is particularly noteworthy. Furthermore, the commercial catalyst faces limitations such as complex deterioration at high temperatures and challenges in product separation, whereas the fixed-bed system employed here allows for efficient catalyst recycling.

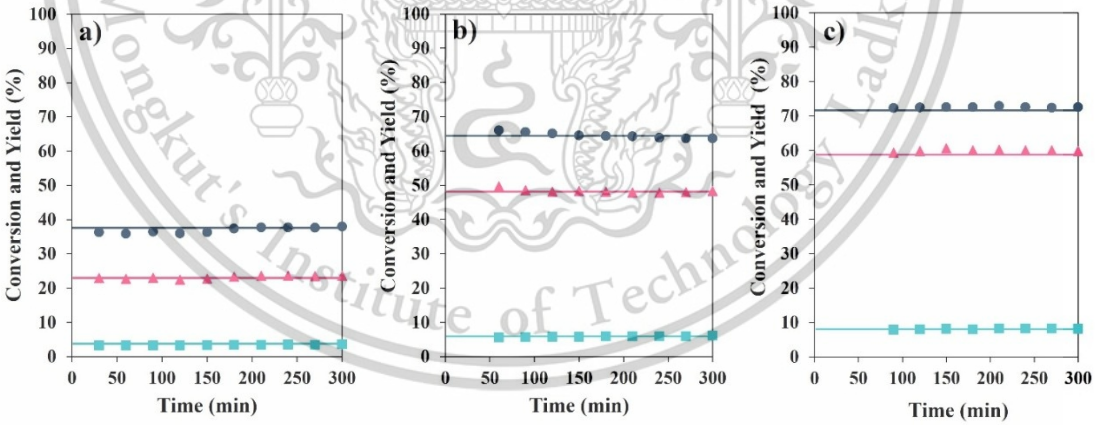

Figure 4.12 Reaction time profile for cross-metathesis of acetylene/ethylene using a) $8WO_3/SiO_2$, b) $8WO_3$/20CuPS-Le and c) $8WO_3$/30CuPS-Le; (●) conversion, (▲) 1,3-butadiene, (■) cyclohexene.

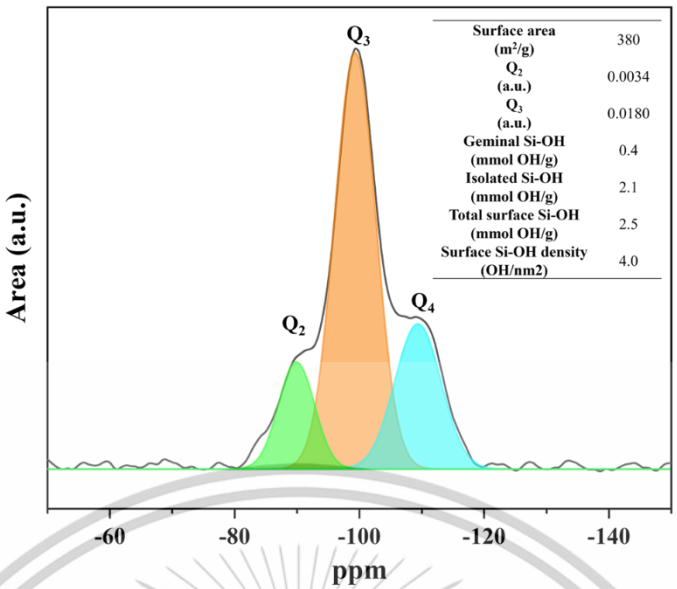

Figure 4.13 ^{29}Si CPMAS NMR spectra and surface silanol density (Insert table) of SiO_2(Davisil)

Table 4.6 Acetylene/ethylene cross-metathesis over WO_3 supported on siliceous supports.

Entry	Catalysts	Catalytic System	Temperature (°C)	Pressure (bar)	Acetylene: Ethylene (v/v)	1,3-Butadiene Production (mmol/h.g_{cat})	1,3-Butadiene Selectivity (%)	Ref.
1	$8WO_3$/30CuPS-Le	Fixed bed	450	1	1:99	6.3	82	This work
2	$7WO_3/SiO_2$(Davisil)	Fixed bed	450	1	1:99	5.5	85	25
3	$5WO_3$/NaY	Fixed bed	450	1	1:99	3.2	86	25
4	$5WO_3$/MCM-41	Fixed bed	450	1	1:99	5.3	85	25
5	$5WO_3$/SBA-15	Fixed bed	450	1	1:99	5.7	85	25
6	Hoveyda–Grubbs second generation catalyst (HG2)	Batch	80	14	1:32	12.5	50	24

Chapter 5
Conclusions and suggestions

5.1 Conclusions

Bio-butadiene can be produced via the cross-metathesis of bioethanol-derived acetylene and ethylene using WO_3 supported on silanol-rich materials prepared from Cu-leached CuPS. The Cu-leaching process generated a higher concentration of surface silanols in CuPS-derived supports compared to fumed SiO_2. As the higher Cu loading (30wt.%) resulted in an increased presence of Cu^{2+} octahedral sites ($Cu^{2+}(Osi)_6$) encapsulated within tetrahedral silica layers, leading to a greater number of exposed isolated and geminal silanols following Cu leaching (30CuPS-Le > 20CuPS-Le > fumed SiO_2). Importantly, CuPS must undergo reduction before Cu leaching to decrease Cu-SiO_2 interactions.

At 5wt.% WO_3 loading, all supports exhibited sufficient surface silanols to accommodate highly dispersed WO_3 species, including single-site and polymeric WO_3. Consequently, a comparable 1,3-butadiene production rate (~4.7 mmol/h·g_{cat}) with high stability was observed for $5WO_3/SiO_2$, $5WO_3$/20CuPS-Le, and 5 WO_3/30CuPS-Le catalysts. However, at 8wt.% WO_3 loading, the limited number of surface silanols in fumed SiO_2 lead to the formation of bulk WO_3, resulting in decreased catalytic activity. In contrast, $8WO_3$/30CuPS-Le retained highly dispersed WO_3 species due to the greater availability of exposed silanols in the Cu-leached 30CuPS support. Hence, the cross-metathesis activity correlated with the relative amounts of exposed silanols available for WO_3 anchoring, following the trend: $8WO_3$/30CuPS-Le (6.3 mmol/h·g_{cat}) > $8WO_3$/20CuPS-Le (5.1 mmol/h·g_{cat}) > $8WO_3/SiO_2$ (2.5 mmol/h·g_{cat}).

5.2 Suggestions

-The influence of WO_3 loading on silanol-rich SiO_2 supports should be further investigated better to understand its influence on WO_3 species and catalytic performance.

-The catalyst stability, reusability, coke formation after reaction, and catalyst performance using larger feedstocks, such as fatty acids should be investigated.

References

[1] N.L. Morrow, The industrial production and use of 1,3-butadiene., Environ. Health Perspect. 86 (1990) 7–8. https://doi.org/10.1289/ehp.90867.

[2] Wm.C. White, Butadiene production process overview, Chem. Biol. Interact. 166 (2007) 10–14. https://doi.org/10.1016/j.cbi.2007.01.009.

[3] R.J. Parod, Butadiene, 1,3-, in: P. Wexler (Ed.), Encycl. Toxicol. Third Ed., Academic Press, Oxford, 2014: pp. 568–571. https://doi.org/10.1016/B978-0-12-386454-3.00368-7.

[4] A. Zanchet, L.N. Carli, M. Giovanela, R.N. Brandalise, J.S. Crespo, Use of styrene butadiene rubber industrial waste devulcanized by microwave in rubber composites for automotive application, Mater. Des. 39 (2012) 437–443. https://doi.org/10.1016/j.matdes.2012.03.014.

[5] T. Sone, Industrial Synthetic Method of the Rubbers. 1. Butadiene Rubber, Int. Polym. Sci. Technol. 43 (2016) 49–54. https://doi.org/10.1177/0307174X1604300110.

[6] alchemist, Butadiene Rubber (BR): Versatile Applications and Advantages, Ascent Petrochem Hold. Co Ltd. (2023). https://www.ascent-petrochem.com/news/butadiene-rubber-br-versatile-applications-and-advantages/ (accessed February 12, 2025).

[7] Butadiene Market Size, Growth, Analysis & Forecast, 2035, Chemanalyst (2023). https://www.chemanalyst.com/industry-report/butadiene-market-623 (accessed February 22, 2024).

[8] T. Ishizaki, M. Usui, S. Kuchiki, M. Hirahara, H. Ogihara, H. Kurokawa, H. Miura, 1,3-Butadiene Production by Simple Dehydrogenation of 1-Butene in the Presence of Steam Over Pt Supported on SnO2-Coated Al2O3, Catal. Lett. 154 (2024) 217–223. https://doi.org/10.1007/s10562-023-04281-7.

[9] F.J. Dumez, G.F. Froment, Dehydrogenation of 1-Butene into Butadiene. Kinetics, Catalyst Coking, and Reactor Design, Ind. Eng. Chem. Process Des. Dev. 15 (1976) 291–301. https://doi.org/10.1021/i260058a014.

[10] V.P. Haribal, Y. Chen, L. Neal, F. Li, Intensification of Ethylene Production from Naphtha via a Redox Oxy-Cracking Scheme: Process Simulations and Analysis, Engineering 4 (2018) 714–721. https://doi.org/10.1016/j.eng.2018.08.001.

[11] D.C. Longstaff, Naphtha Cracking Kinetics and Process Chemistry on Y and ZSM5 Type Catalysts, Energy Fuels 33 (2019) 2445–2452. https://doi.org/10.1021/acs.energyfuels.8b04128.

[12] M.H.M. Ahmed, O. Muraza, S. Nakaoka, A.K. Jamil, A. Mayoral, V. Sebastian, Z.H. Yamani, T. Masuda, Stability Assessment of Regenerated Hierarchical ZSM-48 Zeolite Designed by Post-Synthesis Treatment for Catalytic Cracking of Light Naphtha, Energy Fuels 31 (2017) 14097–14103. https://doi.org/10.1021/acs.energyfuels.7b02796.

[13] M.L. Boyd, T.-M. Wu, M.H. Back, Kinetics of the thermal reactions of ethylene. Part I, Can. J. Chem. 46 (1968) 2415–2426. https://doi.org/10.1139/v68-394.

[14] N.I. Il'chenko, L.Yu. Dolgikh, Single-stage catalytic conversion of ethylene to butadiene, Theor. Exp. Chem. 29 (1994) 245–246. https://doi.org/10.1007/BF00530304.

[15] L.Yu. Dolgikh, N.I. Il'chenko, N.V. Pavlenko, Conversion of ethylene to butadiene and higher hydrocarbons in the absence of a catalyst, Theor. Exp. Chem. 31 (1995) 82–85. https://doi.org/10.1007/BF00529991.

[16] I. Bin Samsudin, H. Zhang, S. Jaenicke, G.-K. Chuah, Recent Advances in Catalysts for the Conversion of Ethanol to Butadiene, Chem. – Asian J. 15 (2020) 4199–4214. https://doi.org/10.1002/asia.202001023.

[17] D. Cespi, F. Passarini, I. Vassura, F. Cavani, Butadiene from biomass, a life cycle perspective to address sustainability in the chemical industry, Green Chem. 18 (2016) 1625–1638. https://doi.org/10.1039/C5GC02148K.

[18] A.P. Kagyrmanova, V.A. Chumachenko, V.N. Korotkikh, V.N. Kashkin, A.S. Noskov, Catalytic dehydration of bioethanol to ethylene: Pilot-scale studies and process simulation, Chem. Eng. J. 176–177 (2011) 188–194. https://doi.org/10.1016/j.cej.2011.06.049.

[19] I. Rossetti, M. Compagnoni, E. Finocchio, G. Ramis, A. Di Michele, Y. Millot, S. Dzwigaj, Ethylene production *via* catalytic dehydration of diluted bioethanol: A step towards an integrated biorefinery, Appl. Catal. B Environ. 210 (2017) 407–420. https://doi.org/10.1016/j.apcatb.2017.04.007.

[20] G. Chen, S. Li, F. Jiao, Q. Yuan, Catalytic dehydration of bioethanol to ethylene over TiO2/γ-Al2O3 catalysts in microchannel reactors, Catal. Today 125 (2007) 111–119. https://doi.org/10.1016/j.cattod.2007.01.071.

[21] F. Jamil, M. Aslam, A.H. Al-Muhtaseb, A. Bokhari, S. Rafiq, Z. Khan, A. Inayat, A. Ahmed, S. Hossain, M.S. Khurram, M.S.A. Bakar, Greener and sustainable production of bioethylene from bioethanol: current status, opportunities and perspectives, Rev. Chem. Eng. 38 (2022) 185–207. https://doi.org/10.1515/revce-2019-0026.

[22] S. Moon, H.-J. Chae, M.B. Park, Dehydration of Bioethanol to Ethylene over H-ZSM-5 Catalysts: A Scale-Up Study, Catalysts 9 (2019) 186. https://doi.org/10.3390/catal9020186.

[23] M. Li, H. Zhao, S. Chen, S. Liu, L. Yan, C. Hou, B. Jiang, Reengineering of the carbon-to-acetylene process featuring negative carbon emission, Green Chem. 25 (2023) 8584–8592. https://doi.org/10.1039/D3GC01775C.

[24] I.-T. Trotuş, T. Zimmermann, N. Duyckaerts, J. Geboers, F. Schüth, Butadiene from acetylene–ethylene cross-metathesis, Chem. Commun. 51 (2015) 7124–7127. https://doi.org/10.1039/C5CC00853K.

[25] P. Promchana, K. Choojun, W. Limphirat, Y. Poo-arporn, T. Sooknoi, Selective acetylene removal from ethylene-rich feed by cross-metathesis over supported WO3 catalysts, Appl. Catal. Gen. 650 (2023) 118972. https://doi.org/10.1016/j.apcata.2022.118972.

[26] S. Watmanee, K. Suriye, P. Praserthdam, J. Panpranot, Formation of isolated tungstate sites on hierarchical structured SiO2- and HY zeolite-supported WOx catalysts for propene metathesis, J. Catal. 376 (2019) 150–160. https://doi.org/10.1016/j.jcat.2019.07.001.

[27] H. Guesmi, R. Grybos, J. Handzlik, F. Tielens, Characterization of tungsten monomeric oxide species supported on hydroxylated silica; a DFT study, RSC Adv. 6 (2016) 39424–39432. https://doi.org/10.1039/C6RA05395E.

[28] X. Dong, X. Ma, H. Xu, Q. Ge, Comparative study of silica-supported copper catalysts prepared by different methods: formation and transition of copper phyllosilicate, Catal. Sci. Technol. 6 (2016) 4151–4158. https://doi.org/10.1039/C5CY01965F.

[29] W. Prasanseang, K. Choojun, Y. Poo-arporn, A.-L. Huang, Y.-C. Lin, T. Sooknoi, Linear long-chain **α**-olefins from hydrodeoxygenation of methyl palmitate over copper phyllosilicate catalysts, Appl. Catal. Gen. 635 (2022) 118555. https://doi.org/10.1016/j.apcata.2022.118555.

[30] D.-T. To, Y.-C. Lin, Copper Phyllosilicates-Derived Catalysts in the Production of Alcohols from Hydrogenation of Carboxylates, Carboxylic Acids, Carbonates, Formyls, and CO2: A Review, Catalysts 11 (2021) 255. https://doi.org/10.3390/catal11020255.

[31] B. Zhang, S. Hui, S. Zhang, Y. Ji, W. Li, D. Fang, Effect of copper loading on texture, structure and catalytic performance of Cu/SiO2 catalyst for hydrogenation of dimethyl oxalate to ethylene glycol, J. Nat. Gas Chem. 21 (2012) 563–570. https://doi.org/10.1016/S1003-9953(11)60405-2.

[32] L. Delaude, A.F. Noels, Metathesis, in: John Wiley & Sons, Inc. (Ed.), Kirk-Othmer Encycl. Chem. Technol., John Wiley & Sons, Inc., Hoboken, NJ, USA, 2005: p. metanoel.a01. https://doi.org/10.1002/0471238961.metanoel.a01.

[33] F. Lefebvre, Y. Bouhoute, K.C. Szeto, N. Merle, A. de Mallmann, R. Gauvin, M. Taoufik, Olefin Metathesis by Group VI (Mo, W) Metal Compounds, in: R. Davarnejad, B. Sajjadi (Eds.), Alkenes, InTech, 2018. https://doi.org/10.5772/intechopen.69320.

[34] J.C. Mol, R. Buffon, Metathesis in Oleochemistry, J. Braz. Chem. Soc. 9 (1998) 1–11. https://doi.org/10.1590/S0103-50531998000100002.

[35] W.M. Haynes, ed., CRC Handbook of Chemistry and Physics, 97th ed., CRC Press, Boca Raton, 2016. https://doi.org/10.1201/9781315380476.

[36] P. Pässler, W. Hefner, K. Buckl, H. Meinass, A. Meiswinkel, H. Wernicke, G. Ebersberg, R. Müller, J. Bässler, H. Behringer, D. Mayer, Acetylene, in: Wiley-VCH (Ed.), Ullmanns Encycl. Ind. Chem., 1st ed., Wiley, 2011. https://doi.org/10.1002/14356007.a01_097.pub4.

[37] H. Zimmermann, R. Walzl, Ethylene, in: Ullmanns Encycl. Ind. Chem., John Wiley & Sons, Ltd, 2009. https://doi.org/10.1002/14356007.a10_045.pub3.

[38] Z. Berk, Chapter 27 - Food packaging, in: Z. Berk (Ed.), Food Process Eng. Technol. Third Ed., Academic Press, 2018: pp. 625–641. https://doi.org/10.1016/B978-0-12-812018-7.00027-0.

[39] H. Lischka, E. Ventura, M. Dallos, The Diels–Alder Reaction of Ethene and 1,3-Butadiene: An Extended Multireference ab initio Investigation, ChemPhysChem 5 (2004) 1365–1371. https://doi.org/10.1002/cphc.200400104.

[40] C.-X. Cui, Y.-J. Liu, A thorough understanding of the Diels–Alder reaction of 1,3-butadiene and ethylene, J. Phys. Org. Chem. 27 (2014) 652–660. https://doi.org/10.1002/poc.3313.

[41] Y. Yoshimura, N. Kijima, T. Hayakawa, K. Murata, K. Suzuki, F. Mizukami, K. Matano, T. Konishi, T. Oikawa, M. Saito, T. Shiojima, K. Shiozawa, K. Wakui, G. Sawada, K. Sato, S. Matsuo, N. Yamaoka, Catalytic Cracking of Naphtha to Light Olefins, Catal. Surv. Jpn. 4 (2001) 157–167. https://doi.org/10.1023/A:1011463606189.

[42] F. Li, L.M. NEAL, J. ZHANG, Redox catalysts for the oxidative cracking of hydrocarbons, methods of making, and methods of use thereof, WO2018049389A1, 2018. https://patents.google.com/patent/WO2018049389A1/en (accessed May 2, 2025).

[43] J.S. Kruger, T. Dong, G.T. Beckham, M.J. Biddy, Integrated conversion of 1-butanol to 1,3-butadiene, RSC Adv. 8 (2018) 24068–24074. https://doi.org/10.1039/C8RA02977F.

[44] I. Choinopoulos, Grubbs' and Schrock's Catalysts, Ring Opening Metathesis Polymerization and Molecular Brushes—Synthesis, Characterization, Properties and Applications, Polymers 11 (2019) 298. https://doi.org/10.3390/polym11020298.

[45] P.D. Nieres, J. Zelin, A.F. Trasarti, C.R. Apesteguía, Heterogeneous catalysis for valorisation of vegetable oils via metathesis reactions: ethenolysis of methyl oleate, Catal. Sci. Technol. 6 (2016) 6561–6568. https://doi.org/10.1039/C6CY01214K.

[46] R.F. Morrison, N. Lipscomb, R.B. Eldridge, P. Ginn, Rhenium Oxide based Olefin Metathesis, Ind. Eng. Chem. Res. 53 (2014) 19136–19144. https://doi.org/10.1021/ie5034232.

[47] W. Phongsawat, B. Netiworaruksa, K. Suriye, S. Dokjampa, P. Praserthdam, J. Panpranot, Role of support nature (γ-Al2O3 and SiO2-Al2O3) on the performances of rhenium oxide catalysts in the metathesis of ethylene and 2-pentene, J. Nat. Gas Chem. 21 (2012) 158–164. https://doi.org/doi:10.1016/S1003-9953(11)60348-4.

[48] K. Bouchmella, M. Stoyanova, U. Rodemerck, D.P. Debecker, P. Hubert Mutin, Avoiding rhenium loss in non-hydrolytic synthesis of highly active Re–Si–Al olefin metathesis catalysts, Catal. Commun. 58 (2015) 183–186. https://doi.org/10.1016/j.catcom.2014.09.024.

[49] D. Zhang, X. Li, K. Liu, S. Huang, X. Zhu, F. Chen, S. Xie, L. Xu, Metathesis of C4 olefin over Mo-based heterogeneous catalysts: A novel route to propene and isopentene, Appl. Catal. Gen. 439–440 (2012) 171–178. https://doi.org/10.1016/j.apcata.2012.07.002.

[50] I. Rodríguez-Ramos, A. Guerrero-Ruiz, N. Homs, P.R. de la Piscina, J.L.G. Fierro, Reactions of propene on supported molybdenum and tungsten oxides, J. Mol. Catal. Chem. 95 (1995) 147–154. https://doi.org/10.1016/1381-1169(94)00017-4.

[51] A. Rybak, P.A. Fokou, M.A.R. Meier, Metathesis as a versatile tool in oleochemistry, Eur. J. Lipid Sci. Technol. 110 (2008) 797–804. https://doi.org/10.1002/ejlt.200800027.

[52] S. Lwin, I.E. Wachs, Olefin Metathesis by Supported Metal Oxide Catalysts, ACS Catal. 4 (2014) 2505–2520. https://doi.org/10.1021/cs500528h.

[53] D.P. Debecker, M. Stoyanova, U. Rodemerck, F. Colbeau-Justin, C. Boissère, A. Chaumonnot, A. Bonduelle, C. Sanchez, Aerosol route to nanostructured WO3-SiO2-Al2O3 metathesis catalysts: Toward higher propene yield, Appl. Catal. Gen. 470 (2014) 458–466. https://doi.org/10.1016/j.apcata.2013.06.041.

[54] S. Lwin, Y. Li, A.I. Frenkel, I.E. Wachs, Nature of WO_x Sites on SiO_2 and Their Molecular Structure–Reactivity/Selectivity Relationships for Propylene Metathesis, ACS Catal. 6 (2016) 3061–3071. https://doi.org/10.1021/acscatal.6b00389.

[55] T.I. Bhuiyan, P. Arudra, M.N. Akhtar, A.M. Aitani, R.H. Abudawoud, M.A. Al-Yami, S.S. Al-Khattaf, Metathesis of 2-butene to propylene over W-mesoporous molecular sieves: A comparative study between tungsten containing MCM-41 and SBA-15, Appl. Catal. Gen. 467 (2013) 224–234. https://doi.org/10.1016/j.apcata.2013.07.034.

[56] E.L. Lee, I.E. Wachs, In Situ Spectroscopic Investigation of the Molecular and Electronic Structures of SiO_2 Supported Surface Metal Oxides, J. Phys. Chem. C 111 (2007) 14410–14425. https://doi.org/10.1021/jp0735482.

[57] N. Habbache, N. Alane, S. Djerad, L. Tifouti, Leaching of copper oxide with different acid solutions, Chem. Eng. J. 152 (2009) 503–508. https://doi.org/10.1016/j.cej.2009.05.020.

[58] H. Yue, Y. Zhao, S. Zhao, B. Wang, X. Ma, J. Gong, A copper-phyllosilicate core-sheath nanoreactor for carbon–oxygen hydrogenolysis reactions, Nat. Commun. 4 (2013) 2339. https://doi.org/10.1038/ncomms3339.

[59] L.-F. Chen, P.-J. Guo, M.-H. Qiao, S.-R. Yan, H.-X. Li, W. Shen, H.-L. Xu, K.-N. Fan, Cu/SiO2 catalysts prepared by the ammonia-evaporation method: Texture, structure, and catalytic performance in hydrogenation of dimethyl oxalate to ethylene glycol, J. Catal. 257 (2008) 172–180. https://doi.org/10.1016/j.jcat.2008.04.021.

[60] Y.-J. Tsou, T.D. To, Y.-C. Chiang, J.-F. Lee, R. Kumar, P.-W. Chung, Y.-C. Lin, Hydrophobic Copper Catalysts Derived from Copper Phyllosilicates in the Hydrogenation of Levulinic Acid to γ-Valerolactone, ACS Appl. Mater. Interfaces 12 (2020) 54851–54861. https://doi.org/10.1021/acsami.0c17612.

[61] J.-W. Jiang, C.-C. Tu, C.-H. Chen, Y.-C. Lin, Highly Selective Silica-supported Copper Catalysts Derived from Copper Phyllosilicates in the Hydrogenation of Adipic Acid to 1,6-hexanediol, ChemCatChem 10 (2018) 5449–5458. https://doi.org/10.1002/cctc.201801580.

[62] Y. Zhao, B. Shan, Y. Wang, J. Zhou, S. Wang, X. Ma, An Effective CuZn–SiO2 Bimetallic Catalyst Prepared by Hydrolysis Precipitation Method for the Hydrogenation of Methyl Acetate to Ethanol, Ind. Eng. Chem. Res. 57 (2018) 4526–4534. https://doi.org/10.1021/acs.iecr.7b05391.

[63] T. Toupance, M. Kermarec, J.-F. Lambert, C. Louis, Conditions of Formation of Copper Phyllosilicates in Silica-Supported Copper Catalysts Prepared by Selective Adsorption, J. Phys. Chem. B 106 (2002) 2277–2286. https://doi.org/10.1021/jp013153x.

[64] C.C. Liu, G.E. Maciel, The Fumed Silica Surface: A Study by NMR, J. Am. Chem. Soc. 118 (1996) 5103–5119. https://doi.org/10.1021/ja954120w.

[65] W. Janssens, E.V. Makshina, P. Vanelderen, F. De Clippel, K. Houthoofd, S. Kerkhofs, J.A. Martens, P.A. Jacobs, B.F. Sels, Ternary Ag/MgO-SiO $_2$ Catalysts for the Conversion of Ethanol into Butadiene, ChemSusChem 8 (2015) 994–1008. https://doi.org/10.1002/cssc.201402894.

[66] Y. Cabrera, A. Cabrera, F.H. Larsen, C. Felby, Solid-state 29Si NMR and FTIR analyses of lignin-silica coprecipitates, Holzforschung 70 (2016) 709–718. https://doi.org/10.1515/hf-2015-0165.

[67] T.I. Bhuiyan, P. Arudra, M.N. Akhtar, A.M. Aitani, R.H. Abudawoud, M.A. Al-Yami, S.S. Al-Khattaf, Metathesis of 2-butene to propylene over W-mesoporous molecular sieves: A comparative study between tungsten containing MCM-41 and SBA-15, Appl. Catal. Gen. 467 (2013) 224–234. https://doi.org/10.1016/j.apcata.2013.07.034.

[68] S. Maksasithorn, P. Praserthdam, K. Suriye, D.P. Debecker, Preparation of super-microporous WO3–SiO2 olefin metathesis catalysts by the aerosol-assisted sol–gel process, Microporous Mesoporous Mater. 213 (2015) 125–133. https://doi.org/10.1016/j.micromeso.2015.04.020.

[69] P.P. González-Borrero, F. Sato, A.N. Medina, M.L. Baesso, A.C. Bento, G. Baldissera, C. Persson, G.A. Niklasson, C.G. Granqvist, A. Ferreira da Silva, Optical band-gap determination of nanostructured WO3 film, Appl. Phys. Lett. 96 (2010) 061909. https://doi.org/10.1063/1.3313945.

[70] E.I. Ross-Medgaarden, I.E. Wachs, Structural Determination of Bulk and Surface Tungsten Oxides with UV–vis Diffuse Reflectance Spectroscopy and Raman Spectroscopy, J. Phys. Chem. C 111 (2007) 15089–15099. https://doi.org/10.1021/jp074219c.

[71] Y. Wu, L. Fan, W. Huang, S. Chen, S. Chen, F. Chen, C. Zou, Z. Wu, Depressed transition temperature of $W_x V_{1-x} O_2$: mechanistic insights from the X-ray absorption fine structure (XAFS) spectroscopy, Phys. Chem. Chem. Phys. 16 (2014) 17705. https://doi.org/10.1039/C4CP01661K.

[72] X. Carrier, E. Marceau, H. Carabineiro, V. Rodríguez-González, M. Che, EXAFS spectroscopy as a tool to probe metal–support interaction and surface molecular structures in oxide-supported catalysts: application to Al2O3-supported Ni(ii) complexes and ZrO2-supported tungstates, Phys. Chem. Chem. Phys. 11 (2009) 7527. https://doi.org/10.1039/b822969d.

[73] A. Kuzmin, J. Purans, X-ray absorption spectroscopy study of the local environment around tungsten and molybdenum ions in tungsten-phosphate and molybdenum-phosphate glasses, Proc SPIE 2968 (1997) 180–185. https://doi.org/10.1117/12.266831.

[74] J. Handzlik, M. Gierada, K. Kurleto, Role of Surface Silanols in Active Site Formation during Olefin Metathesis over a WOx/SiO2 Catalyst: A Computational Perspective, J. Phys. Chem. C 128 (2024) 5934–5946. https://doi.org/10.1021/acs.jpcc.4c01305.

[75] W. Schulze, S. Schwalbe, K. Trepte, A. Croy, J. Kortus, S. Gräfe, Bond formation insights into the Diels–Alder reaction: A bond perception and self-interaction perspective, J. Chem. Phys. 158 (2023) 164102. https://doi.org/10.1063/5.0145555.

[76] C. Santato, M. Odziemkowski, M. Ulmann, J. Augustynski, Crystallographically Oriented Mesoporous WO 3 Films: Synthesis, Characterization, and Applications, J. Am. Chem. Soc. 123 (2001) 10639–49. https://doi.org/10.1021/ja011315x.

[77] J.G. Howell, Y.-P. Li, A.T. Bell, Propene Metathesis over Supported Tungsten Oxide Catalysts: A Study of Active Site Formation, ACS Catal. 6 (2016) 7728–7738. https://doi.org/10.1021/acscatal.6b01842.

[78] S. Wanqing, R. Zhang, X. Bai, Q. Jia, H. Ji, Exposed crystal facets of WO3 nanosheets by phase control on NO2-sensing performance, J. Mater. Sci. Mater. Electron. 31 (2020) 610–620. https://doi.org/10.1007/s10854-019-02565-6.

[79] E.L. Lee, I.E. Wachs, In Situ Raman Spectroscopy of SiO2-Supported Transition Metal Oxide Catalysts: An Isotopic 18O–16O Exchange Study, J. Phys. Chem. C 112 (2008) 6487–6498. https://doi.org/10.1021/jp076485w.

Appendix

Appendix A

Calculation

A1. Acetylene conversion

$$\%\text{Conversion} = \frac{\text{mol of acetylene}_0 - \text{mol of acetylene}_t}{\text{mol of acetylene}_0} \times 100$$

A2. Product yield

$$\%\text{Yield} = \frac{\text{mol of product A}_t}{\text{mol of acetylene}_0} \times 100$$

A3. Product selectivity

$$\%\text{Selectivity} = \frac{\text{Yield of product A (\%)}}{\text{Acetylene conversion (\%)}} \times 100$$

A4. Catalyst activity

$$\text{Catalyst activity } (\text{mmol}_{feed}/\text{h}\cdot\text{g}_{cat}) = \frac{\text{mmol of converted acetylene (mmol/h)}}{\text{weight of catalyst (g)}}$$

A5. 1,3-Butadiene production rate

$$\text{Production rate } (\text{mmol/h}\cdot\text{g}_{cat}) = \frac{\text{mmol of 1,3-butadiene production (mmol/h)}}{\text{weight of catalyst (g)}}$$

A5. Material balance

$$\text{Material balance} = \frac{\text{Total yield of product (\%)}}{\text{Acetylene conversion (\%)}} \times 100$$

A6. Relative amount of Si-OH

$$\text{Relative amount of Si-OH} = \text{Integral area}_{support}\text{(a.u.)} - \text{Integral area}_{8\text{wt.\% } WO_3 \text{ catalysts}}\text{(a.u.)}$$

A7. %Relative amount of Si-OH for WO_3

$$\% \text{ Si-OH for } WO_3 = \frac{\text{Integral area}_{support}(\text{a.u.}) - \text{Integral area}_{8\text{wt.\% } WO_3 \text{ catalysts}}(\text{a.u.})}{\text{Integral area}_{support}(\text{a.u.})}$$

Author Biography

Name	Kanokwan Wengwirat
Date of Birth	21 August 1999
Address	780 Phatthanakan 30, Suan Luang Subdistrict, Suan Luang District, Phatthanakan Road, Bangkok
Education	(2020) Bachelor of Science Program in Industrial Chemistry, King Mongkut's Institute of Technology Ladkrabang
Publication	Bio-derived butadiene from Cross-metathesis over Silanol rich WO_3 catalysts obtained from Copper Phyllosilicate, Kanokwan Wengwirat, Kittisak Choojun, Pratya Promchana, Wanwisa Limphirat, and Tawan Sooknoi, Catalysis Science & Technology, 2025